ARTICLE

Ultra-high mobility transparent organic thin film transistors grown by an off-centre spin-coating method

Yongbo Yuan[1], Gaurav Giri[2], Alexander L. Ayzner[2,3], Arjan P. Zoombelt[2], Stefan C. B. Mannsfeld[3], Jihua Chen[4], Dennis Nordlund[3], Michael F. Toney[3], Jinsong Huang[1] & Zhenan Bao[2]

Organic semiconductors with higher carrier mobility and better transparency have been actively pursued for numerous applications, such as flat-panel display backplane and sensor arrays. The carrier mobility is an important figure of merit and is sensitively influenced by the crystallinity and the molecular arrangement in a crystal lattice. Here we describe the growth of a highly aligned meta-stable structure of 2,7-dioctyl[1]benzothieno[3,2-b][1]benzothiophene (C8-BTBT) from a blended solution of C8-BTBT and polystyrene by using a novel off-centre spin-coating method. Combined with a vertical phase separation of the blend, the highly aligned, meta-stable C8-BTBT films provide a significantly increased thin film transistor hole mobility up to $43\,cm^2\,Vs^{-1}$ ($25\,cm^2\,Vs^{-1}$ on average), which is the highest value reported to date for all organic molecules. The resulting transistors show high transparency of $>90\%$ over the visible spectrum, indicating their potential for transparent, high-performance organic electronics.

[1] Department of Mechanical and Materials Engineering and Nebraska Center for Materials and Nanoscience, University of Nebraska-Lincoln, Lincoln, Nebraska 68588-0656, USA. [2] Department of Chemical Engineering, Stanford University, Stanford, California 94305, USA. [3] Stanford Synchrotron Radiation Lightsource, SLAC National Accelerator Laboratory, Menlo Park, California 94025, USA. [4] Center for Nanophase Materials Sciences, Oak Ridge National Laboratory, Oak Ridge, Tennessee 37831-6494, USA. Correspondence and requests for materials should be addressed to J.H. (email: jhuang2@unl.edu) or to Z.B. (email: zbao@stanford.edu).

Transparent organic semiconductors with high charge-carrier mobilities have been an important research target due to their broad applications in flat-panel displays[1,2], radio-frequency identification tags[3,4], complementary integrated circuits[5-7] and biological and medical applications[8-13]. The carrier mobility of organic semiconductor films is strongly influenced by the crystallinity, molecular packing structures of the organic thin films and charge traps at the gate dielectric/semiconductor interface[14-17]. Because of the small van der Waals interaction between organic molecules, the crystallinity, grain size and crystal alignment of the solution-processed organic thin films have been shown to be very sensitive to the fabrication conditions, such as solvent evaporation rate[18], and liquid surface tension force[19,20]. In addition to the changed thin film morphology, certain molecular organic semiconductors can form various molecular packing structures (polymorphs) by changing film formation processes[19,20]. Since the electronic wavefunction overlap that determines the charge transfer integral is a very sensitive function of the precise molecular packing, the various polymorphs generally have different carrier mobilities with some having a higher mobility than their equilibrium structures[10,19-23].

In this manuscript, we report the formation of a highly aligned, meta-stable crystal packing structure (likely a polymorph) of 2,7-dioctyl[1]benzothieno[3,2-b][1]benzothiophene (C8-BTBT by a simple off-centre spin-coating (OCSC) method, wherein C8-BTBT and polystyrene (PS) blend solution was used to result in simultaneously a passivation effect of the dielectric surface as well as improving the continuity of the thin C8-BTBT film. An ultra-high maximum hole mobility of $43 \, cm^2 \, Vs^{-1}$ and an average hole mobility of $25 \, cm^2 \, Vs^{-1}$ were obtained, much higher than the previously reported average hole mobility of $3 \sim 16 \, cm^2 \, Vs^{-1}$ (refs 18,24-26).

Results

OCSC and device transparency. The organic thin film transistors (OTFTs) were fabricated on either highly doped silicon substrates or transparent indium tin oxide (ITO) coated glass substrates with a bottom-gate top-contact structure (Fig. 1a). A crosslinked poly(4-vinylphenol) (PVP) was used as the gate dielectric layer (Supplementary Fig. 1)[27]. The semiconductor channel layer was deposited by an OCSC method, in which the substrate is placed away from the centre of the spin-coater (Fig. 1b and Supplementary Fig. 2), using a blend of C8-BTBT with an insulating PS. Since all the organic materials used here have large bandgaps, the resulting films when cast on ITO substrates showed an excellent transparency of >90% in the visible region (Fig. 1c), which is comparable to the best transparencies reported to date for TFTs, including both organic and metal oxide TFTs[28,29]. Such highly transparent transistors are of great interest for flat-panel display backplane and sensor array applications.

Formation of highly aligned meta-stable C8-BTBT films. In the OCSC process, the centrifugal force is almost unidirectional over the whole substrate. This method produced highly aligned C8-BTBT crystals, as confirmed by their distinct anisotropic optical absorption spectra under varying polarization of incident light. The peak absorbance of the C8-BTBT film formed by the OCSC method is 2.5 times stronger when the light polarization direction is perpendicular to the radial direction as compared with the radial direction (Fig. 1d). In contrast, the C8-BTBT films fabricated by conventional on-centre spin-coating (i.e., substrate centre sitting at the centre of spin-coater axis) showed nearly isotropic light absorption, indicating that crystals in the film were randomly oriented in the plane of the substrate (Fig. 1e). There was a small spectral shift of $\sim 50 \, meV$ between the peak positions

of the first absorption band for the two different polarizations in the OCSC film (Fig. 1d), which corresponds to the Davydov splitting of the lowest energy transition in the isolated molecule induced by the anisotropic crystal environment. The C8-BTBT crystals formed by the OCSC method all have a small but distinct blue shift of $\sim 20 \, meV$ in the absorption spectrum onset as compared with C8-BTBT crystals prepared through other methods, such as small-angle drop-coating (Fig. 1d and Supplementary Methods)[18,30]. The spectral differences are indicative of a change in the crystal packing of C8-BTBT.

To test whether the OCSC film has a meta-stable crystal structure, we measured absorption spectra before and after solvent vapour annealing (o-dichlorobenzene, DCB, Fig. 1f) and thermal annealing (90 °C for 3 h, Fig. 1g). Both processes resulted in a red-shift of the absorption onset, and the shifted spectra become similar to the spectra obtained from small-angle drop-cast films (Supplementary Methods). In addition, we observed that the spectra of the OCSC films were unchanged after being stored at room temperature for more than 1 month (Supplementary Fig. 3) or being annealed at temperatures below 80 °C for 3 h, indicating a long lifetime for the meta-stable film (Fig. 1g). Interestingly, it was also noticed that the preferred growth direction of the OCSC film is along the (010) direction of the C8-BTBT crystal (Supplementary Note 1 and Supplementary Fig. 4), which is different from what previously reported, i.e., (100) or (110) directions being the preferred growth direction[24,25].

To further support the meta-stable phase and the high crystallinity of C8-BTBT, we performed two-dimensional (2D) grazing incidence X-ray diffraction (GIXD) experiments. The observation of an 18th order out-of-plane (11L) Bragg peak from the OCSC processed thin film (10–20 nm) strongly indicated the highly crystalline nature of our films (Fig. 2a)[18]. The in-plane coherence length by Scherrer analysis provided a lower bound crystallite size of $\sim 100 \, nm$. This crystal coherence length is a lower bound value, as sample degradation and peak broadening occurred with X-ray beam exposure (Supplementary Fig. 5). In contrast, the Bragg peaks of the on-centre spin-coated C8-BTBT films were generally broader, with peak widths corresponding to smaller crystallite sizes (<20 nm). Moreover, in the on-centre spin-coated films, GIXD intensities on the right and left sides of the image are identical, confirming that the crystallites form a 2D powder in the plane of the substrate. In contrast, the observed asymmetric pattern in the OCSC film (Supplementary Fig. 6 and Supplementary Note 2) is an indication of the strong in-plane alignment, and is consistent with the optical absorption spectra. Strong evidence for a new crystal packing structure is derived from the presence of an additional diffraction peak near the (002) Bragg reflection, where the lower $Q_z \sim 0.44 \, Å^{-1}$ is in agreement with the (002) plane spacing reported for the equilibrium crystal[31], while the higher $Q_z \sim 0.46 \, Å^{-1}$ is strong evidence for a new polymorph (Fig. 2b). This higher Q_z peak is from a meta-stable phase since it disappears, or decreases in intensity, after thermal annealing (Fig. 2b and Supplementary Fig. 7). In addition, the clear (11L) Bragg peaks shift in position after thermal annealing (Fig. 2c) from $Q_{xy} = 1.34 \, Å^{-1}$ (meta-stable) to $1.32 \, Å^{-1}$ (equilibrium), indicating a smaller intermolecular spacing along (110) direction in the meta-stable phase. The peak shift has previously been observed for other meta-stable systems as well[19]. The meta-stable (002) Bragg ($Q_z \sim 0.46 \, Å^{-1}$) peak is also present in the on-centre spin-coated samples; however, the crystallite size is too small to give high hole carrier mobilities. Unfortunately, we are unable to obtain the crystal structure for these meta-stable films due to beam degradation of the sample upon long X-ray exposure times required to get accurate meta-stable peak positions and intensities (Supplementary Fig. 5).
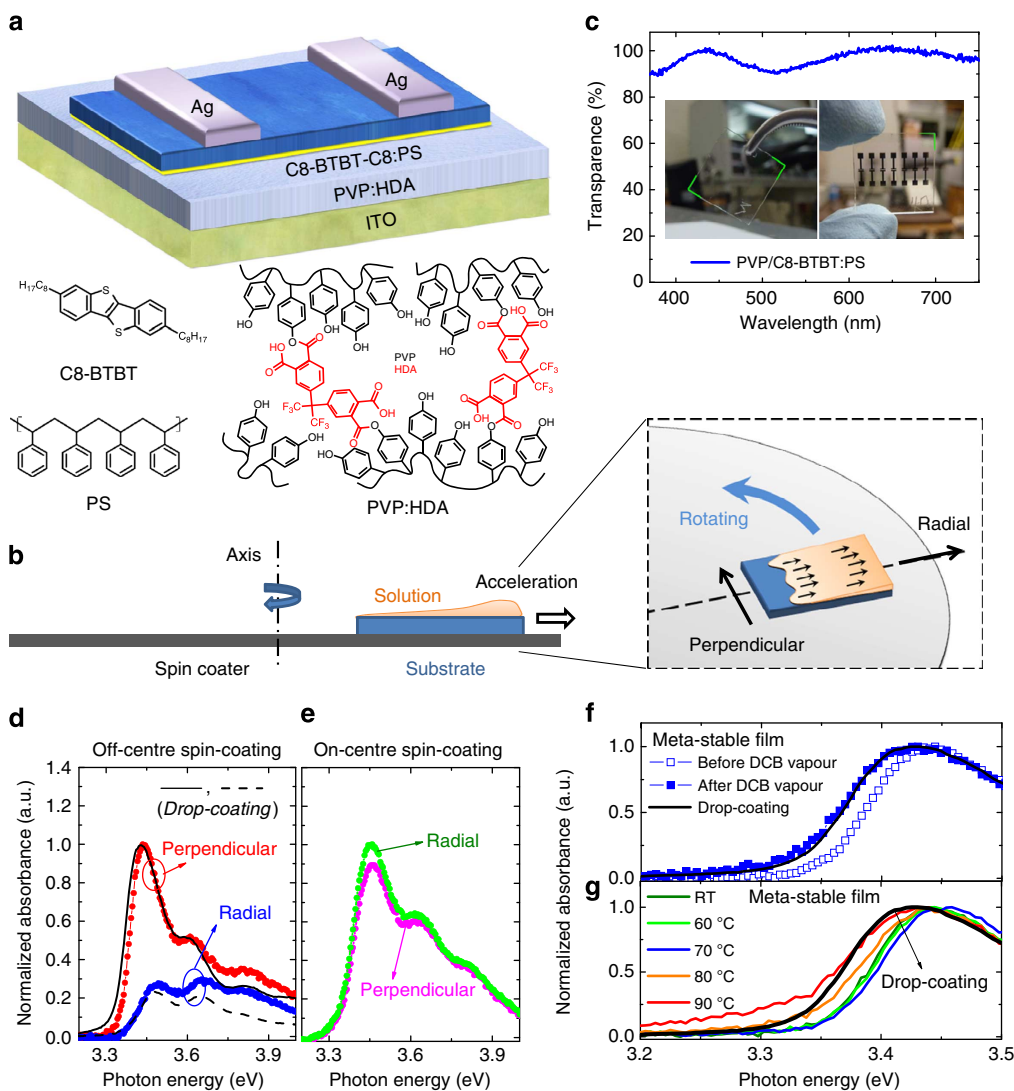
Figure 1 | Highly aligned meta-stable C8-BTBT:PS film fabricated by OCSC method. (**a**) Schematic device configuration of OTFT with C8-BTBT:PS blends as channel layer, PVP:HDA as dielectric layer and ITO as the gate electrode; the chemical structures of C8-BTBT, PS, PVP and HDA are shown. (**b**) Schematic illustration of the OCSC process, in which the substrates are located away from the axis of the spin-coater. (**c**) Transmission spectrum of the PVP:HDA/C8-BTBT:PS film. Inset: photographs of C8-BTBT:PS film and corresponding OTFT device with a structure of glass/ITO/PVP:HDA/C8-BTBT:PS. (**d**) Normalized polarized-absorption spectrum of OCSC C8-BTBT:PS film, where the light electrical field is in radial (blue circles) or perpendicular direction (red circles). The two directions are marked in the Fig. 1b; for comparison, the absorption peak of C8-BTBT film prepared by small-angle drop-coating, according to literature procedures[25], is also shown (**d,f,g**, dark line). (**e**) Normalized polarized-absorption spectrum of on-centre spin-coated C8-BTBT:PS film, where the light electrical field is in radial (green circles) or perpendicular direction (pink circles). (**f**) Perpendicular polarized-absorption spectrum of meta-stable C8-BTBT:PS film before and after DCB vapour annealing. (**g**) Perpendicular polarized-absorption spectrum of meta-stable C8-BTBT:PS film after thermal annealing for 3 h at each temperature.

Since sample degradation currently precludes the full solution of the unit cell and molecular packing, we additionally characterized our highly aligned films using Near-edge X-ray Absorption Fine-Structure (NEXAFS) Spectroscopy. Figure 3 shows NEXAFS spectra for C8-BTBT films where the incidence angle of the highly polarized synchrotron X-rays was varied relative to the (100) direction (defined as orthogonal, Fig. 3a and Supplementary Fig. 8) and the (010) direction (defined as parallel, Fig. 3b). Similar results were obtained from C8-BTBT:PS films (Supplementary Fig. 9). The peaks near 285 eV correspond to transition from the C1s core-level to antibonding π^* orbitals of the conjugated backbone, where the intensity depends on the angle between the electric field vector and the direction of the final state (π^*) orbitals[32]. The data show significant incident angular dependence and azimuthal anisotropy (difference

between the two different sample orientations with respect to the beam). This shows a large degree of molecular order, an upright geometry (the π^* signal is strongest at 90°), and an overall in-plane crystal alignment (the π^* signal is strongest with electric field vector along radial direction). The observed high in-plane alignment in NEXAFS is consistent with the anisotropic optical absorption spectra (Fig. 1d) and GIXD images (Supplementary Fig. 4). In Fig. 3c, the integrated π^* intensity from 283.0 to 286.3 eV is plotted versus the incidence angle of the parallel and orthogonal condition, respectively. By comparison with simulations according to the formalism for anisotropic NEXAFS intensity for a π^* vector outlined by Stohr and Outka[32], a transition dipole moment (TDM) tilt angle (the angle between TDM and the normal direction of substrate plane, Supplementary Fig. S8) of about $88 \pm 3°$ was obtained.
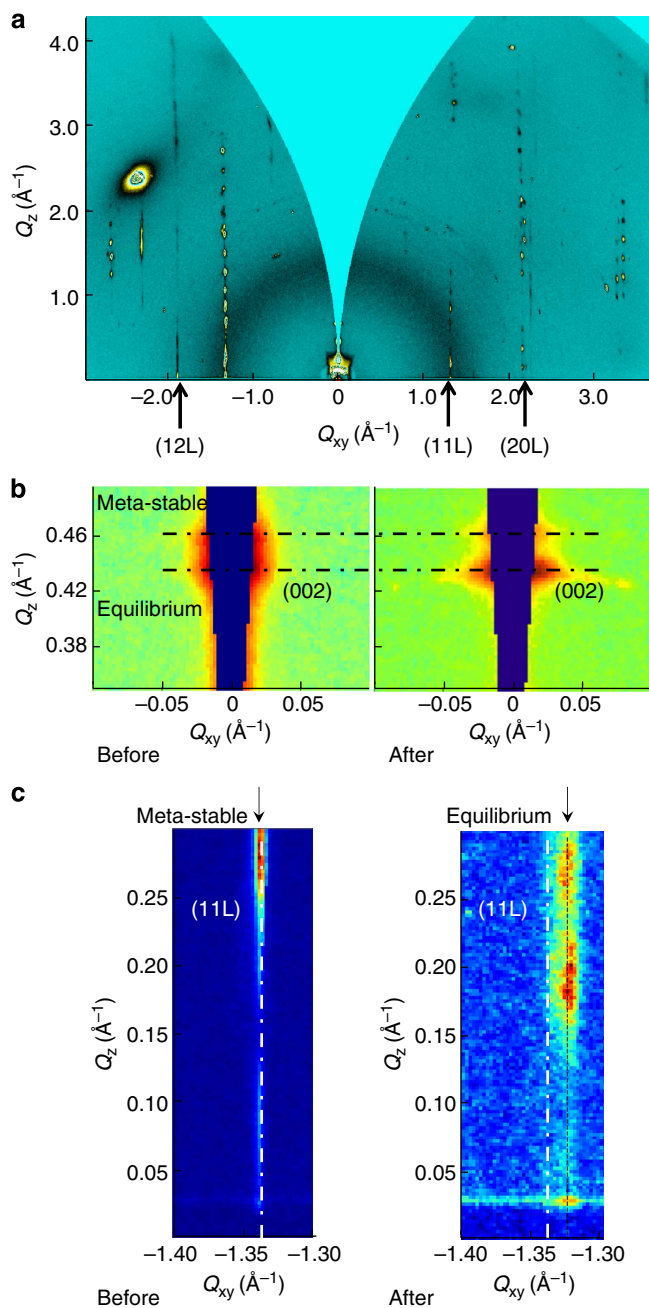
Figure 2 | GIXD investigations of highly aligned, meta-stable C8-BTBT films. (**a**) GIXD images of an OCSC C8-BTBT samples. The presence of the asymmetric pattern is indicative of a high degree of in-plane alignment. The high order Bragg peaks indicate good crystallinity. There is an artifact due to the substrate at $Q_{xy} = -2.1 \, \text{Å}^{-1}$ and $Q_z = 2.1 \, \text{Å}^{-1}$. (**b**) GIXD images of the (002) Bragg peaks of OCSC C8-BTBT:PS film obtained before and after thermal annealing, where the peak related to the meta-stable phase (top peak, $Q_{xy} \sim 0.46 \, \text{Å}^{-1}$) is less intense compared with that from the equilibrium phase (bottom peak, $Q_{xy} \sim 0.44 \, \text{Å}^{-1}$) after the thermal anneal. (**c**) GIXD images of the (11L) Bragg peaks of OCSC C8-BTBT:PS film obtained before and after thermal annealing. The in-plane position of (11L) Bragg peaks shifted after the film was heated to above 90 °C and was subsequently cooled down to room temperature. The (11L) Bragg peaks first disappeared while the (00L) peaks remained visible, indicating the formation of a liquid crystalline phase (Supplementary Fig. 7b). The (11L) Bragg peaks then reformed as the film was cooled, but the (11L) peak shifted away from the original position, implying that the Bragg peak before heating was caused by a meta-stable phase.
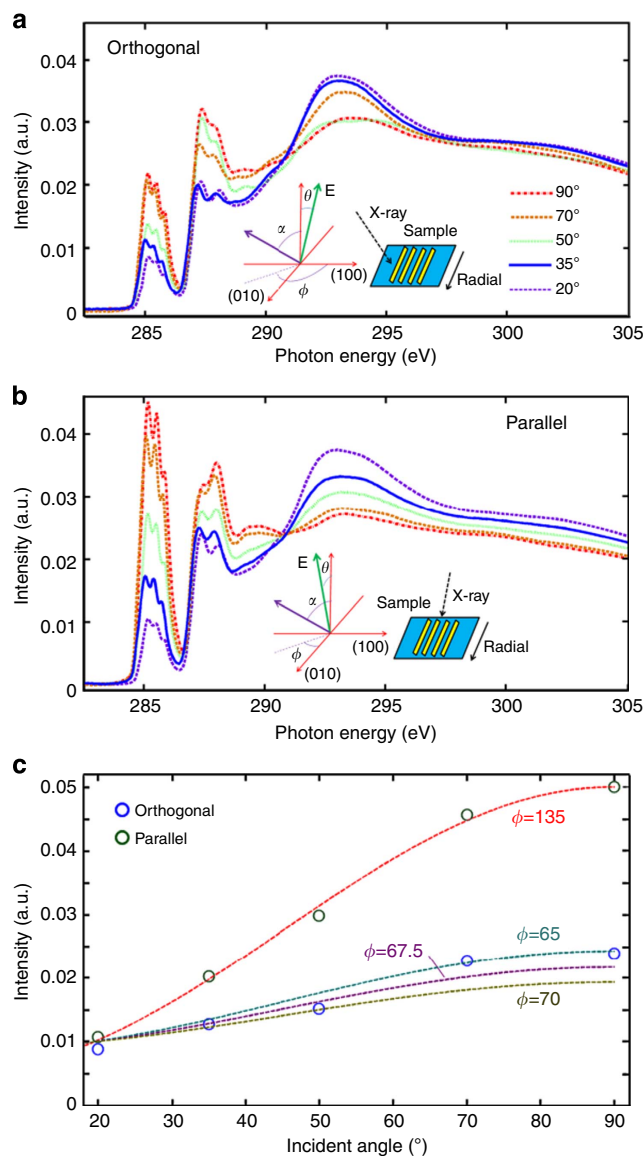

Figure 3 | NEXAFS investigations of C8-BTBT in-plane alignment. (**a**) Carbon K edge NEXAFS spectra for the C8-BTBT:PS films at different X-ray incidence angles (θ, i.e., the angle between the X-ray electric field E and the normal direction of the substrate plane, where an incident angle of 90° means the incident electric field is in the plane of the substrate. The orientation of the TDM is defined by the polar tilt angle α and the azimuthal angle ϕ). The lower energy features centred around 285 eV correspond to electronic transitions from core orbitals to antibonding $\pi^{\star}$ orbitals, whereas the higher energy feature centred around 293 eV correspond to the transitions to unbound $\sigma^{\star}$ orbitals. Inset illustration shows the incident electric field of the polarized X-ray is orthogonal to the radial direction. (**b**) Corresponding NEXAFS spectra for the C8-BTBT:PS films with the incident electric field of the polarized X-ray being parallel to the radial direction. (**c**) Intensities of the $\pi^{\star}$ transitions versus incidence angle. $\pi^{\star}$ peaks were spectrally integrated from 283.0 to 286.3 eV, which is shown for both relative sample orientations (orthogonal and parallel) with respect to the incident polarization. The dash lines are the fitting curves with different azimuthal angle ϕ.
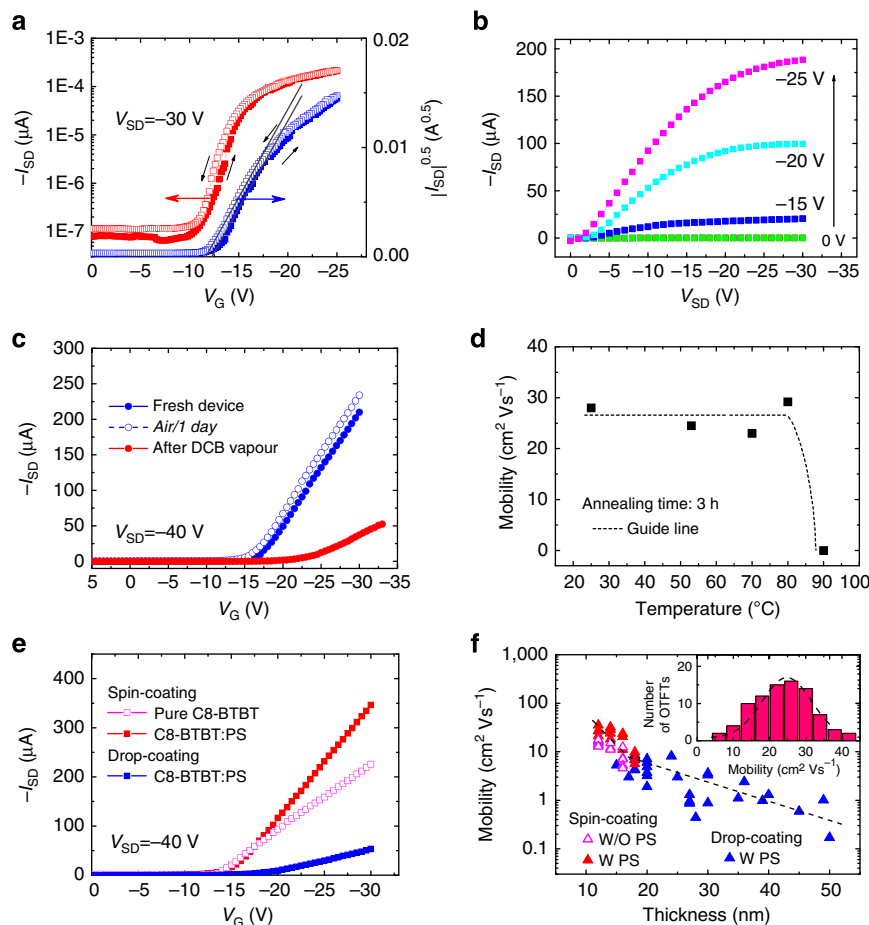
Figure 4 | High-performance OTFT devices with OCSC C8-BTBT:PS films. (**a**) Transfer and (**b**) Output characteristics of an OTFT prepared by OCSC with C8-BTBT:PS film as a channel layer. The channel length is 100 μm, channel width is 1 mm and the capacitance of the dielectric is 1.2×10^{-4} F m^{-2}. (**c**) DCB vapour annealing for 2.5 h decreases the channel current. The channel current for the device kept in air for 1 day is also shown, excluding the possible explanation of device instability. (**d**) Hole carrier mobilities after thermal annealing for 3 h at each temperature. (**e**) Comparison of channel current of OTFT with OCSC channel layer or large-angle drop-coated channel layer. (**f**) Influence of the channel layer thickness and PS blending on the hole mobility. Inset: mobility distribution of the OCSC-prepared OTFTs.

(Supplementary Figs 9,10 and Supplementary Note 3). This is larger than that of the on-centre spun samples, which gave a TDM tilt angle of $77 \sim 81°$ (Supplementary Fig. 11), suggesting a different molecular packing structure between off-centre spun films and conventionally on-centre spun films.

Hole mobilities in the OCSC C8-BTBT films. We investigated the hole transport characteristics of the OTFTs made with OCSC films (Fig. 4). These films showed an extremely high maximum hole mobility of 43 cm^2 Vs^{-1} for saturation mobility and 20 cm^2 Vs^{-1} for linear mobility. The average saturation mobility is 25 cm^2 Vs^{-1} (in set of Fig. 4f). It should be noted that strikingly high saturation mobilities of $90 \sim 118$ cm^2 Vs^{-1} were observed several times in some samples and the transfer current curves were shown in Supplementary Fig. 13. However, due to the lack of reproducibility, we report the maximum of 43 cm^2 Vs^{-1} here as we observed similar value ($35 \sim 43$ cm^2 Vs^{-1}) in around 10% of more than 80 devices fabricated. These mobilities are the highest reported values for small-molecular organic semiconductors to date[18,19,33–35]. The high channel current of these devices has been independently verified by three research laboratories (Supplementary Fig. 14).

Discussion

The higher mobilities we obtained here is unlikely to be only attributed to a larger grain size as compared with previous studies, where single crystals were used in the channels[18,24,25]. Several additional factors may be contributing to the extremely high mobility: the highly aligned crystalline thin film, more continuous formation of C8-BTBT film due to the presence of the PS layer, passivation effect of the PS and possibly the meta-stable packing structure. While our films are highly aligned (Fig. 3 and Supplementary Figs 4,15), the higher mobility values do not originate from the intrinsic anisotropic change transport in the C8-BTBT crystal. This is because the mobilities along the radial and perpendicular directions were measured to be the same in absence of visible grain boundaries or cracks (Supplementary Fig. 16). The observed isotropic mobility is reasonable because the charge transfer integrals along different directions are roughly balanced[16,24]. However, the high degree of alignment will still be a contributing factor to the high mobility value because such an alignment reduces the grain boundary scattering[30].

The hole mobility of C8-BTBT has a strong dependence on the film thickness. Two coating methods, OCSC and large-angle drop-coating, were used to tune the C8-BTBT thickness within a range of 10–50 nm. The OCSC films have typical thicknesses

from 10 to 18 nm, while the large-angle drop-coating films are around 15–50 nm. In contrast to the formation of the thick C8-BTBT crystals film in Figs 1b, a much larger tilting angle was used in the large-angle drop-coating process to reduce the C8-BTBT thickness to be 15–50 nm (Supplementary Methods). Independent of the two coating method, thinner films resulted in higher mobilities (Fig. 4e,f) in both cases, while the OCSC films showed the highest mobilities.

Second, we observed that blending PS into C8-BTBT yielded significantly higher mobilities (Fig. 4e,f and Supplementary Fig. 17). The higher mobility with PS may be due to enhanced inter-grain connectivity, because the increased solution viscosity helped to form more continuous films, as has been observed with other small molecule/polymer blends[36,37]. Another important contributing factor is the vertical phase separation, which generally occurs in polymer and small molecule blends[36,38] and would result in reduced surface traps in our devices. To verify the vertical phase separation between C8-BTBT and PS, we studied the films with transmission electron microscopy (TEM) cross-sectional images, where the samples were prepared by being embedded in epoxy resin and microtomed into 70-nm-thick slices. In conventional (unfiltered) cross-sectional TEM view (Fig. 5a), the C8-BTBT film is visible as a dark thin layer, due to its high crystallinity and electron density. An additional thinner layer (≤ 5 nm) is visible in places between the C8-BTBT layer and

the substrate, which we attribute to the PS layer. We further confirmed the existence of this ultrathin PS layer by using energy-filtered TEM (Fig. 5b). The 22 ± 4 eV image utilized the plasmon peak of the p-type organic semiconductor to enhance the contrast in the electron energy loss spectra, and the thickness map is obtained from the ratio of unfiltered and filtered image, yielding pixel by pixel values of t/λ, where t is film thickness in nanometre and λ is the electron mean free pathway. Both the 22 ± 4 eV image and the thickness map suggest that there is indeed an additional layer underneath C8-BTBT[39,40]. Further indication of vertical phase separation in the C8-BTBT:PS film was observed by scanning electron microscopy using a thicker film with a higher percentage of PS, showing a similar phase-separated structure, where the PS layer was sandwiched between the C8-BTBT and PVP film (Fig. 5c). The vertical phase separation between C8-BTBT and PS is explained by their different surface energies. The PS segregation to the PVP surface is energetically more favourable than the segregation of C8-BTBT to the PVP surface, because the methyl-terminated C8-BTBT has lower surface energy than either PVP or PS (Supplementary Note 4).

Covering the PVP surface with an ultrathin layer of PS could reduce the interface traps caused by the polar hydroxyl groups on the PVP chain, contributing to the observed higher mobility[41,42]. Previously, the higher mobility in small molecule/polymer blends was also attributed to the 'zone refinement effect' during the vertical phase separation process, and this purification effect may also be present in this case[43,44]. Furthermore, the lower dielectric constant of PS ($\varepsilon_r = 2.6$) than PVP ($\varepsilon_r = 4.2$) provides a less polar environment at the dielectric/C8-BTBT interface, leading to a less energetic disorder in the dielectric[45]. Both effects are expected to result in a higher OTFT mobility.

Finally, the meta-stable molecular packing in the OCSC film is also a contributing factor to the high mobility as can be seen from the much higher mobility of OCSC film compared with the similarly highly aligned drop-cast film (Supplementary Table 1). The presence of meta-stable packing was clearly supported by the peak shift in GIXD and the relaxation of the peak and shifting of the absorption spectrum to the equilibrium phase features. However, its contribution was difficult to quantify. For example, solvent annealing caused relaxation of the meta-stable polymorph (Figs 1f,g and 2c) accompanied by a hole mobility drop from $\sim 26 \, \text{cm}^2 \text{Vs}^{-1}$ to below $4.1 \, \text{cm}^2 \text{Vs}^{-1}$ (Fig. 4c,d). However, the crystal alignment was also disrupted (Supplementary Fig. 7), making it difficult to attribute the mobility drop entirely to crystal structure change. Moreover, the beam damage during GIXD measurements made it impossible to obtain the precise crystal packing structure for the meta-stable polymorph. Therefore, we were not able to determine the impact of the meta-stable packing on transfer integral.

It is not surprising that the ultra-high mobility achieved in the OCSC films combines the contributions from multiple effects. At current stage, it is difficult to pin-point the contribution of each factor quantitatively.

Given that we measured very high hole carrier mobilities in TFTs with highly aligned meta-stable C8-BTBT films, it is important to verify that the devices are robust with respect to bias stress. The performance of OTFTs fabricated with meta-stable C8-BTBT film was found to be quite stable under DC bias at room temperature. A source-drain current of $100 \, \mu\text{A}$ can be maintained under a DC gate bias of -15 V for over 1,000 s (Fig. 6), which indicates that the meta-stable C8-BTBT films did not undergo a relaxation to the equilibrium phase during continuous current flow. In addition, the low bias stress effect also indicates a negligible trap density in meta-stable C8-BTBT films, which can be attributed to the highly crystalline nature of the film and the presence of few grain boundaries as well as the
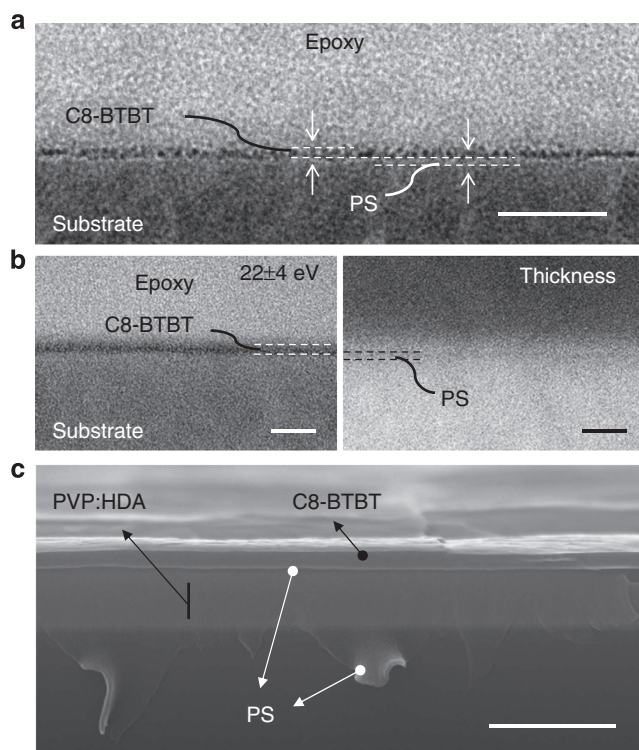
Figure 5 | Vertical phase separation between C8-BTBT and PS. (**a**) Cross-sectional TEM of C8-BTBT:PS film without energy filtering. In an unfiltered cross-sectional TEM view, C8-BTBT film is visible as a dark thin layer with 10–20 nm thickness, due to its high crystallinity and electron density. The scale bar is 100 nm. (**b**) Cross-sectional TEM of C8-BTBT:PS film with energy filtering. Both 22 ± 4 eV image and thickness map suggest that there is an additional layer underneath C8-BTBT. The two scale bars are 50 nm. (**c**) Cross-sectional scanning electron microscopy (SEM) image of thick C8-BTBT:PS film drop coated on PVP surface, where the PS is more flexible than the C8-BTBT crystal and extended out of the cross section, demonstrating the PS segregation is energetically more favourable than the C8-BTBT segregation to the PVP surface. The scale bar is 1 μm.
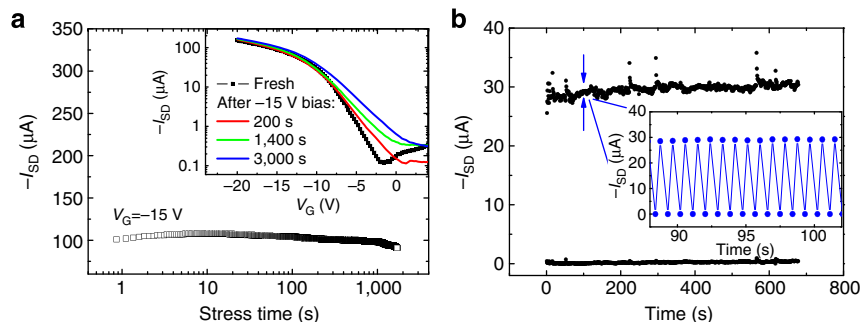
Figure 6 | Bias stress stability of the high mobility C8-BTBT:PS devices. (**a**) Stability of the channel current under a continuous bias stress of -15 V for over 1,000 s, inset show the I_{SD}-V_G curve taken before and after bias stress. (**b**) Cycle stability of the device, where a train of gate voltage pulse (-10 V) was applied and the device was switched between on and off for ~ 750 cycles (1 Hz). Inset show the detail I_{SD} response at the 90th seconds.

interfacial trap passivation by the ultrathin PS layer[41,42,46,47]. After a bias stress of over 200 s, the threshold voltage started to decrease (Fig. 6a, inset). The origin of this shift is not yet fully understood; we hypothesize that this could be related to the motion of ions in the organic layer or the adsorption of moisture at the crosslinked PVP/C8-BTBT interface[48,49]. But the I_{SD} difference caused by the continuous bias becomes negligible when the I_{SD} exceeds 10 μA. The transistor also showed good cycle stability under repeated gate voltage pulses (~ 1 Hz). The I_{SD} remains constant after 750 cycles of switching (Fig. 6b). Podzorov and coworkers[50] have shown that the measured hole mobility of C8-BTBT is highly dependent on the gate voltage sweep rate: slowing down the gate voltage sweep rate decreased the mobility from 1 cm^2 Vs^{-1} to 0.05 cm^2 Vs^{-1}. This sweep rate-dependent mobility results from the presence of trap states, which cause a strong concomitant stress bias effect. In this study, the device showed a negligible trap state density and thus robust stress bias stability, and no obvious sweep rate-dependent mobility was observed (Supplementary Fig. 18).

In summary, we have demonstrated a record high hole mobility of 43 cm^2 Vs^{-1} in OCSC C8-BTBT:PS films (the highest value obtained for small-molecular organic semiconductors) with transparency $>90\%$ in the visible range. The OCSC films were considerably thinner than what previously studied and have meta-stable structure. These meta-stable films were observed to maintain its structural integrity up to 80 °C, and the subsequent fabricated devices were stable under both DC and AC bias at room temperature. Our data indicate that the obtained very high hole mobility in C8-BTBT:PS blend films mainly results from the highly aligned crystalline grains with a slightly reduced in-plane intermolecular spacing. The obtained mobility also clearly benefited from PS blending via the formation of vertical phase separation, where the PS segregated to the dielectric/semiconductor interface may have helped to reduce interfacial traps. Collectively, this study demonstrates a new method to enhance the performance of OTFTs. The highest obtained hole mobility is comparable to that of the polycrystalline silicon, indicating a bright future for OTFT applications.

Methods

Device fabrication. For the device fabrication, either ITO-coated glass substrates or highly doped silicon wafers were used. The substrates were first scrubbed with a brush dipped in acetone and ultrasoniced in pure water, acetone and isopropyl alcohol, respectively. Then these substrates were dried in oven at 80 °C. After UV-ozone treatment, the ITO layer was covered by a low temperature cross-linkable PVP dielectric layer according to literature procedures[27]. Here 4,4′-(hexafluoroisopropylidene)diphthalic anhydride (HDA) was used as the cross linker. The PVP-HDA layer was spin-coated from a 100 mg ml^{-1} solution of PVP:HDA (10:1 by wt) in propylene glycol monomethyl ether acetate. The PVP:HDA films were cured at 100 °C for 60 min to promote the cross-linking

reaction, resulting in a dielectric layer thickness of ~ 330 nm and a measured capacitance of 1.2×10^{-4} F m^{-2} (Supplementary Fig. 1).

The organic semiconductor films were deposited in an nitrogen inert atmosphere on PVP-HDA-coated ITO substrate from a 5 mg ml^{-1} C8-BTBT (or C8-BTBT:PS) solution in DCB via a OCSC method (Supplementary Fig. 2a), where the substrate (15 × 15 mm^2) was placed with its centre away from the rotation axis of the spin-coater at a distance of 20–40 mm. During the OCSC process, the spin speed was gradually increased to 2,700 r.p.m. (Supplementary Fig. 2b). The C8-BTBT crystals grow gradually from one side to the other side in the radial direction. The sample was brought out of the N$_2$-golve box immediately after spin-coating. The C8-BTBT:PS semiconductor layer fabricated on the PVP surface had an thickness of 10–18 nm, which was varied by changing both spin-coating speed and the solution concentration. Finally, silver (Ag) source and drain electrodes were thermally evaporated through a Si shadow mask with a channel length of 100 μm and a channel width of 1 mm, respectively. The electrical characteristics of the devices were measured with two computer-controlled Keithley 2400 source metre in ambient conditions.

Polarized absorption spectroscopy measurement. For the polarized absorption spectrum measurements, the C8-BTBT (or C8-BTBT:PS) films were spin coated on PVP:HDA covered quartz with a size of about 25 × 25 mm^2. Absorption was measured with a UV-Visible spectrophotometer (Thermo Scientific, Evolution 201) combined with a polarizer. The size of the light spot was about 1 × 3 mm^2. The stability of the meta-stable C8-BTBT:PS film was characterized by optical absorption spectroscopy with the polarization of light in the perpendicular direction (Supplementary Fig. 3). The absorption spectrum of the meta-stable C8-BTBT:PS film was collected multiple times over the course of 1 month storage, during which the C8-BTBT:PS film was kept in the dark at ambient conditions. All the optical measurements were carried out on the same region of the film, with a positional error of about 1∼2 mm.

GIXD measurement. GIXD was performed at the Stanford Synchrotron Radiation Lightsource (SSRL) on beamlines 11-3 and 7-2. The photon energy was 12.73 keV in beamline 11-3 and 8 keV in beamline 7-2. The scattering intensity was recorded on a 2D image plate (MAR-345) with a pixel size of 150 μm (2,300 × 2,300 pixels), located at a distance of either 150 mm or 400 mm from the sample centre for beamline 11-3, and with a point detector for beamline 7-2. The distance between the sample and the detector was calibrated using lanthanum hexaboride (LaB$_6$) polycrystalline standard (beamline 11-3). The incidence angle was chosen in the range of 0.10°–0.14°. The beam size was 50 × 150 μm (vertically and horizontally), which resulted in a 150 μm wide beam footprint on the sample that spanned the length of the 2∼3 mm sample. The data were distortion-corrected (theta-dependent image distortion introduced by planar detector surface) before performing quantitative analysis on the images. Numerical integration of the diffraction peak areas was performed with the software WxDiff[51]. The overall resolution in the GIXD experiments, largely determined by the sample size (2-3 mm), was about 0.01 Å^{-1}.

NEXAFS measurement. NEXAFS measurements were performed at the bending magnet beamline 8-2 of SSRL[52], with a ring current of 500 mA, operating the spherical grating monochromator with the 500 l mm^{-1} grating at intermediate (~ 0.3 eV) resolution. The toroidal refocusing optics provided a near circular beam cross-section of about 1 mm FWHM (full width at half maximum) in diameter (footprint horizontally was 1–3 mm FWHM pending on the incidence angle). All the samples were mounted in a single load to an aluminium sample holder using conductive carbon, and all the measurements were performed at room temperature and under ultra-high vacuum conditions (below 10^{-8} Torr). Both the total electron yield and the Auger electron yield were recorded by means of the sample

drain current (measured via a stanford research systems (SRS) current amplifier without bias) and a ϕ 15–255 G double-pass cylindrical mirror analyser operated in pulse counting mode and at a fixed kinetic energy of 257 eV at 200 eV pass energy. Total electron yield was chosen for the analysis in this work. After dark current subtraction, the sample current was normalized to the incoming photon flux, recorded from a freshly Au-evaporated gold mesh that intercepts $\sim 20\%$ of the beam upstream of the chamber. A linear pre-edge background signal was then subtracted, and the spectra were normalized to the total area. The polarization factor P (defined as the ratio of the in-plane component to the total intensity) of the elliptically polarized synchrotron radiation was assumed to be 90% (ref. 32).

TEM Measurement. For cross-section TEM experiments, the sample films were embedded in low viscosity epoxy and microtomed into thin slices with a thickness of 50–100 nm. TEM experiments were performed in a Zeiss Libra 120 which is equipped with an in-column energy filter. An acceleration voltage of 120 kV was used along with an emission current as small as 5×10^{-6} A and a minimal beam intensity to avoid electron beam induced morphological change. To examine the nanomorphology of C8-BTBT:PS films across the thickness direction, cross-sectional TEM samples were prepared by embedding the sample films in epoxy resin and microtoming into 70-nm-thick slices.

References

1. Rogers, J. A. & Bao, Z. Printed plastic electronics and paperlike displays. *J. Polym. Sci., Part A: Polym. Chem.* **40**, 3327–3334 (2002).
2. Gelinck, G. H. *et al.* Flexible active-matrix displays and shift registers based on solution-processed organic transistors. *Nat. Mater.* **3**, 106–110 (2004).
3. Subramanian, V. *et al.* Progress toward development of all-printed RFID tags: materials, processes, and devices. *Proc. IEEE* **93**, 1330–1338 (2005).
4. Baude, P. *et al.* Pentacene-based radio-frequency identification circuitry. *Appl. Phys. Lett.* **82**, 3964–3966 (2003).
5. Klauk, H., Zschieschang, U., Pflaum, J. & Halik, M. Ultralow-power organic complementary circuits. *Nature* **445**, 745–748 (2007).
6. Sirringhaus, H. *et al.* High-resolution inkjet printing of all-polymer transistor circuits. *Science* **290**, 2123–2126 (2000).
7. Crone, B. *et al.* Large-scale complementary integrated circuits based on organic transistors. *Nature* **403**, 521–523 (2000).
8. Someya, T., Dodabalapur, A., Huang, J., See, K. C. & Katz, H. E. Chemical and physical sensing by organic field-effect transistors and related devices. *Adv. Mater.* **22**, 3799–3811 (2010).
9. Lipomi, D. J. *et al.* Skin-like pressure and strain sensors based on transparent elastic films of carbon nanotubes. *Nat. Nanotech.* **6**, 788–792 (2011).
10. Mannsfeld, S. C. *et al.* Highly sensitive flexible pressure sensors with microstructured rubber dielectric layers. *Nat. Mater.* **9**, 859–864 (2010).
11. Kuribara, K. *et al.* Organic transistors with high thermal stability for medical applications. *Nat. Commun.* **3**, 723 (2012).
12. Roberts, M. E. *et al.* Water-stable organic transistors and their application in chemical and biological sensors. *Proc. Natl Acad. Sci. USA* **105**, 12134–12139 (2008).
13. Berggren, M. & Richter-Dahlfors, A. Organic bioelectronics. *Adv. Mater.* **19**, 3201–3213 (2007).
14. Brédas, J.-L., Beljonne, D., Coropceanu, V. & Cornil, J. Charge-transfer and energy-transfer processes in π-conjugated oligomers and polymers: a molecular picture. *Chem. Rev.* **104**, 4971–5004 (2004).
15. Sokolov, A. N. *et al.* From computational discovery to experimental characterization of a high hole mobility organic crystal. *Nat. Commun.* **2**, 437 (2011).
16. Takimiya, K., Shinamura, S., Osaka, I. & Miyazaki, E. Thienoacene-based organic semiconductors. *Adv. Mater.* **23**, 4347–4370 (2011).
17. Yuan, Y. *et al.* Solution-processed nanoparticle super-float-gated organic field-effect transistor as un-cooled ultraviolet and infrared photon counter. *Sci. Rep.* **3**, 2707 (2013).
18. Minemawari, H. *et al.* Inkjet printing of single-crystal films. *Nature* **475**, 364–367 (2011).
19. Giri, G. *et al.* Tuning charge transport in solution-sheared organic semiconductors using lattice strain. *Nature* **480**, 504–508 (2011).
20. Diao, Y. *et al.* Solution coating of large-area organic semiconductor thin films with aligned single-crystalline domains. *Nat. Mater.* **12**, 665–671 (2013).
21. Ruiz, R. *et al.* Structure of pentacene thin films. *Appl. Phys. Lett.* **85**, 4926–4928 (2004).
22. Gundlach, D., Jackson, T., Schlom, D. & Nelson, S. Solvent-induced phase transition in thermally evaporated pentacene films. *Appl. Phys. Lett.* **74**, 3302–3304 (1999).
23. Yoshida, H., Inaba, K. & Sato, N. X-ray diffraction reciprocal space mapping study of the thin film phase of pentacene. *Appl. Phys. Lett.* **90**, 181930 (2007).
24. Soeda, J. *et al.* Solution-crystallized organic field-effect transistors with charge-acceptor layers: high-mobility and low-threshold-voltage operation in air. *Adv. Mater.* **23**, 3309–3314 (2011).
25. Liu, C. *et al.* Solution-processable organic single crystals with bandlike transport in field-effect transistors. *Adv. Mater.* **23**, 523–526 (2011).
26. Uemura, T., Hirose, Y., Uno, M., Takimiya, K. & Takeya, J. Very high mobility in solution-processed organic thin-film transistors of highly ordered [1] benzothieno [3, 2-b] benzothiophene derivatives. *Appl. Phys. Express* **2**, 111501–111503 (2009).
27. Roberts, M. E. *et al.* Cross-linked polymer gate dielectric films for low-voltage organic transistors. *Chem. Mater.* **21**, 2292–2299 (2009).
28. Nomura, K. *et al.* Room-temperature fabrication of transparent flexible thin-film transistors using amorphous oxide semiconductors. *Nature* **432**, 488–492 (2004).
29. Park, S. H. K. *et al.* Transparent and photo-stable zno thin-film transistors to drive an active matrix organic-light-emitting-diode display panel. *Adv. Mater.* **21**, 678–682 (2009).
30. Rivnay, J. *et al.* Large modulation of carrier transport by grain-boundary molecular packing and microstructure in organic thin films. *Nat. Mater.* **8**, 952–958 (2009).
31. Izawa, T., Miyazaki, E. & Takimiya, K. Molecular ordering of high-performance soluble molecular semiconductors and re-evaluation of their field-effect transistor characteristics. *Adv. Mater.* **20**, 3388–3392 (2008).
32. Stöhr, J. & Outka, D. Determination of molecular orientations on surfaces from the angular dependence of near-edge x-ray-absorption fine-structure spectra. *Phys. Rev. B* **36**, 7891 (1987).
33. Takeya, J. *et al.* Very high-mobility organic single-crystal transistors with in-crystal conduction channels. *Appl. Phys. Lett.* **90**, 102120 (2007).
34. Jurchescu, O. D., Baas, J. & Palstra, T. Effect of impurities on the mobility of single crystal pentacene. *Appl. Phys. Lett.* **84**, 3061–3063 (2004).
35. Li, H. *et al.* High-mobility field-effect transistors from large-area solution-grown aligned c60 single crystals. *J. Am. Chem. Soc.* **134**, 2760–2765 (2012).
36. Smith, J. *et al.* Solution-processed organic transistors based on semiconducting blends. *J. Mater. Chem.* **20**, 2562–2574 (2010).
37. Kang, J., Shin, N., Jang, D. Y., Prabhu, V. M. & Yoon, D. Y. Structure and properties of small molecule − polymer blend semiconductors for organic thin film transistors. *J. Am. Chem. Soc.* **130**, 12273–12275 (2008).
38. Hamilton, R. *et al.* High-performance polymer-small molecule blend organic transistors. *Adv. Mater.* **21**, 1166–1171 (2009).
39. Chen, J. *et al.* Ternary behavior and systematic nanoscale manipulation of domain structures in P3HT/PCBM/P3HT-b-PEO films. *J. Mater. Chem.* **22**, 13013–13022 (2012).
40. Drummy, L. F. *et al.* Molecular-scale and nanoscale morphology of P3HT: PCBM bulk heterojunctions: energy-filtered TEM and low-dose HREM. *Chem. Mater.* **23**, 907–912 (2010).
41. Baeg, K. J., Noh, Y. Y., Sirringhaus, H. & Kim, D. Y. Controllable shifts in threshold voltage of top-gate polymer field-effect transistors for applications in organic nano floating gate memory. *Adv. Funct. Mater.* **20**, 224–230 (2010).
42. Park, B. *et al.* Enhanced hole mobility in ambipolar rubrene thin film transistors on polystyrene. *Appl. Phys. Lett.* **92**, 133302 (2008).
43. Chung, Y. S. *et al.* Zone-refinement effect in small molecule − polymer blend semiconductors for organic thin-film transistors. *J. Am. Chem. Soc.* **133**, 412–415 (2010).
44. Li, Y. *et al. In situ* purification to eliminate the influence of impurities in solution-processed organic crystals for transistor arrays. *J. Mater. Chem. C* **1**, 1352–1358 (2013).
45. Sirringhaus, H. Device physics of solution-processed organic field-effect transistors. *Adv. Mater.* **17**, 2411–2425 (2005).
46. Klauk, H. *Organic Electronics: Materials, Manufacturing, and Applications* (Wiley-VCH, 2006).
47. Chang, J. B. & Subramanian, V. Effect of active layer thickness on bias stress effect in pentacene thin-film transistors. *Appl. Phys. Lett.* **88**, 233513 (2006).
48. Kumaki, D., Umeda, T. & Tokito, S. Influence of HO and O on threshold voltage shift in organic thin-film transistors: deprotonation of SiOH on SiO gate-insulator surface. *Appl. Phys. Lett.* **92**, 093309 (2008).
49. Kim, C. S., Lee, S., Gomez, E. D., Anthony, J. E. & Loo, Y.-L. Solvent-dependent electrical characteristics and stability of organic thin-film transistors with drop cast bis (triisopropylsilylethynyl) pentacene. *Appl. Phys. Lett.* **93**, 103302 (2008).
50. Chen, Y. *et al.* Dynamic character of charge transport parameters in disordered organic semiconductor field-effect transistors. *Phys. Chem. Chem. Phys.* **14**, 14142–14151 (2012).
51. Mannsfeld, S. C., Tang, M. L. & Bao, Z. Thin film structure of triisopropylsilylethynyl-functionalized pentacene and tetraceno [2, 3-b] thiophene from grazing incidence X-Ray diffraction. *Adv. Mater.* **23**, 127–131 (2011).
52. Tirsell, K. G. & Karpenko, V. P. A general purpose sub-kev x-ray facility at the stanford synchrotron radiation laboratory. *Nucl. Instrum. Methods Phys. Res. Sect. A* **291**, 511–517 (1990).

Author contributions

J.H. and Z.B. conceived the project and designed the experiments. Y.Y. designed the off-centre spin-coating method, carried out all the device fabrication and characterizations, the optical absorption measurement, SEM, and related data analysis. G.G. and S.C.B.M. carried out the GIXD measurements and molecular structure analysis. A.A. and Y.Y. carried out the data analysis of the optical absorption measurements. A.L.A., D.N. and M.T. carried out the NEXAFS measurements and data analysis. J.C. carried out the TEM measurement. A.P.Z. synthesized the C8-BTBT material. All the authors analysed and interpreted the data and wrote the paper.

Additional information

**Supplementary Information** accompanies this paper at http://www.nature.com/naturecommunications

Competing financial interests: The authors declare no competing financial interests.

Reprints and permission information is available online at http://npg.nature.com/reprintsandpermissions/

How to cite this article: Yuan, Y. *et al.* Ultra-high mobility transparent organic thin film transistors grown by an off-centre spin-coating method. *Nat. Commun.* 5:3005 doi: 10.1038/ncomms4005 (2014).
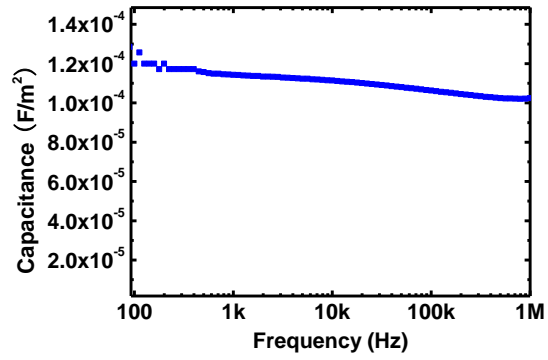
Supplementary Figure 1 | Dependence of the capacitace of PVP:HDA dielectric layer with frequency. The PVP:HDA (~330 nm) was fabricated according to literature procedures.[27]
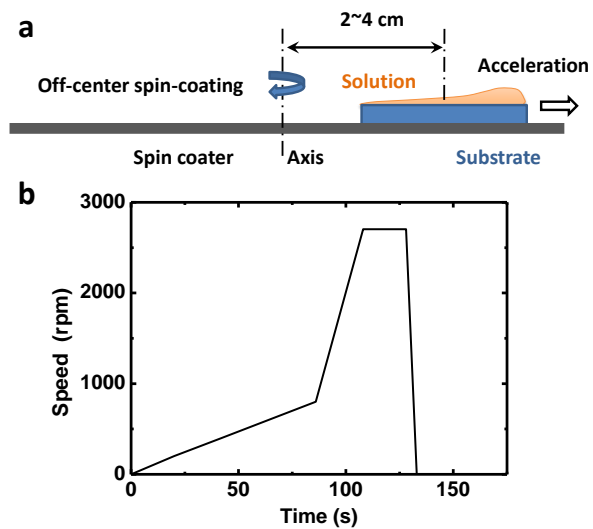
Supplementary Figure 2 | OCSC fabrication process. (**a**) Schematic illustration of the OCSC process; (**b**) Details of a typical spin speed ramp during the OCSC process.
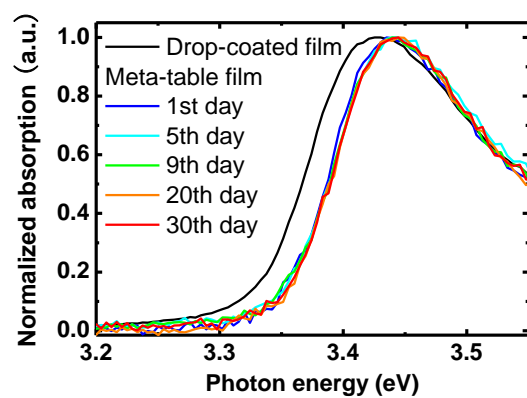
Supplementary Figure 3 | Stability of the polarized absorption spectrum of meta-stable C8-BTBT:PS film at RT. The absorption spectrum of meta-stable C8-BTBT:PS film was different with that of the equilibrium C8-BTBT:PS film (drop-coated film) and did not show any peak shifts for one month.
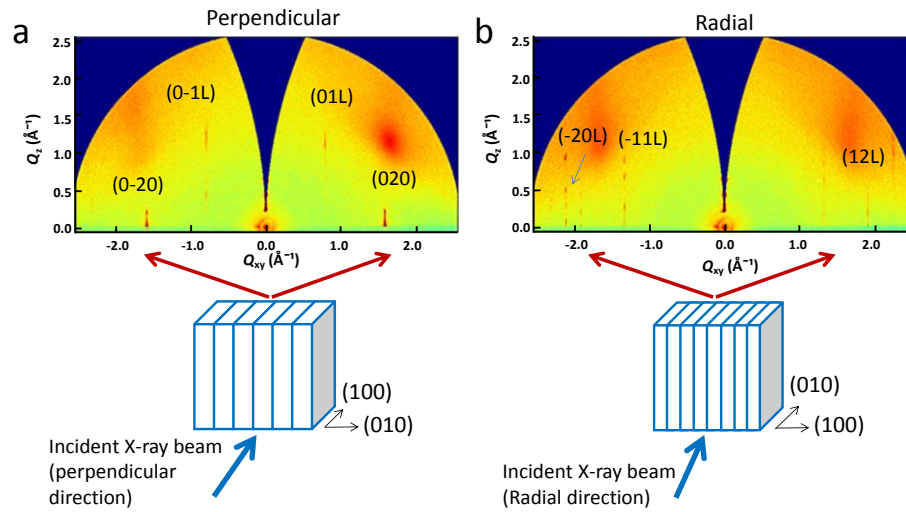
Supplementary Figure 4 | Identification of the (100) and (010) direction. GIXD images with incident X-ray beam along: (**a**) perpendicular direction; (**b**) radial direction, which shows the (100) crystal direction and (010) direction is oriented along the perpendicular and radial directions of casting, respectively.
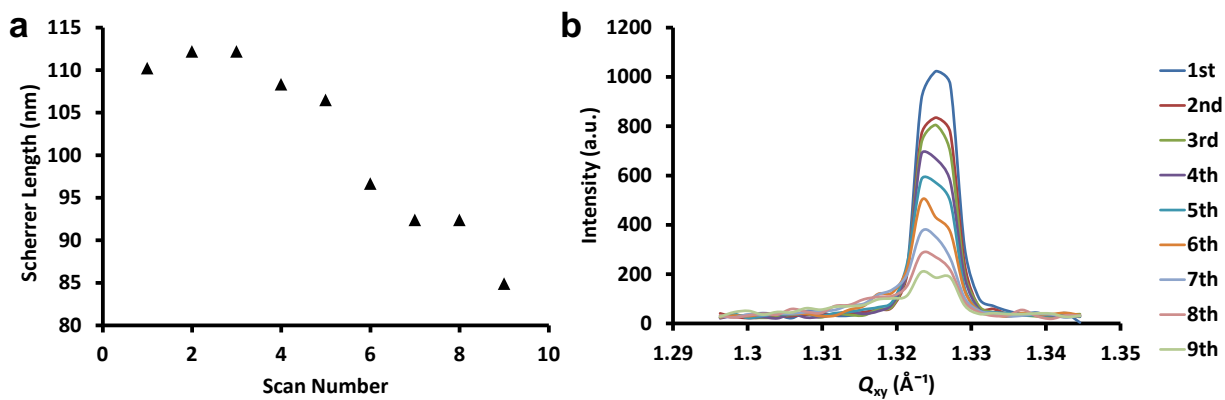
Supplementary Figure 5 | Decay of the meta-stable C8-BTBT film under X-ray beam. (**a**) Change in calculated Scherrer length upon successive scans using the (111) Bragg peak. Each scan exposed the sample to 1 min of X-ray beam. (**b**) Decrease in diffracted intensity of the (111) Bragg peak with repeated X-ray scans. Each scan exposed the sample to 1 min of X–ray beam in the same spot.

a On-center spin-coating

b Off-center spin-coating

Q_{xy} (Å^{-1})

Q_{xy} (Å^{-1})
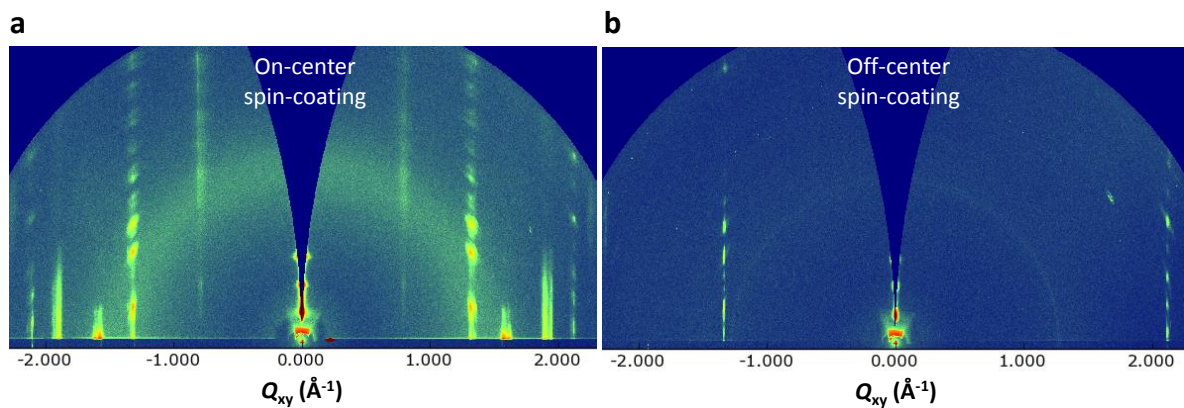
Supplementary Figure 6 | GIXD image of C8-BTBT:PS blended samples fabricated by different spin-coating method. (**a**) on-center spin-coating, and (**b**) off-center spin-coating.
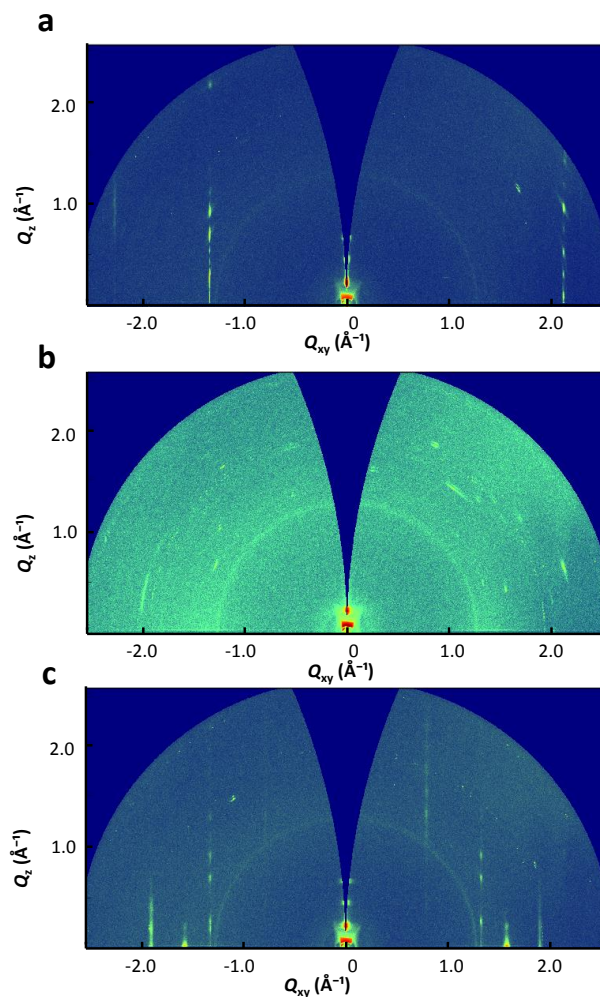
Supplementary Figure 7 | GIXD image of OCSC C8-BTBT:PS film subjected to thermal anneal. (**a**) Original GIXD image. Note the lack of symmetry across $Q_{xy}= 0$, indicating oriented crystals. (**b**) Film heated to 90 ℃. Lack of in plane Bragg peaks show that sample crystallinity is not present. (**c**) Reformed film after cooling to room temperature. The peaks are now more symmetric than that in **a**, implying a less oriented (in-plane) sample that has reformed into a crystalline phase.
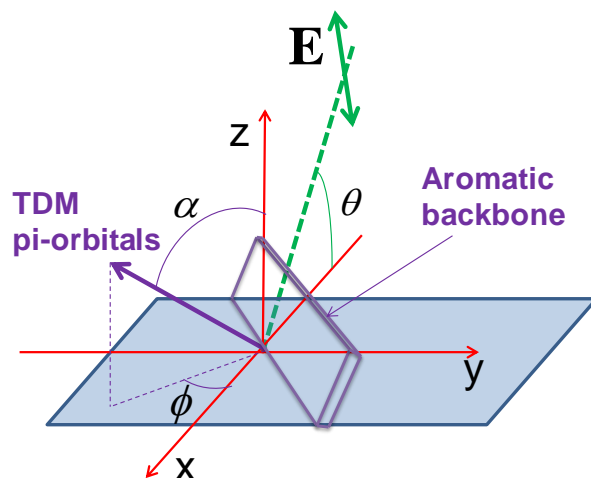
Supplementary Figure 8 | Orientation of the transition dipole moment (TDM). The TDM is normal to the conjugated core of the molecule, specified by the polar (tilt) angle α and the azimuthal angle ϕ. The tilt angle of the conjugated core, measured with respect to the surface normal, is 90-α. The incidence angle of the X-ray electric field **E** is θ, and the absorption intensity is proportional to the square of the scalar product between **E** and the TDM. The dominant polarization component of **E** lies in the x-z plane.
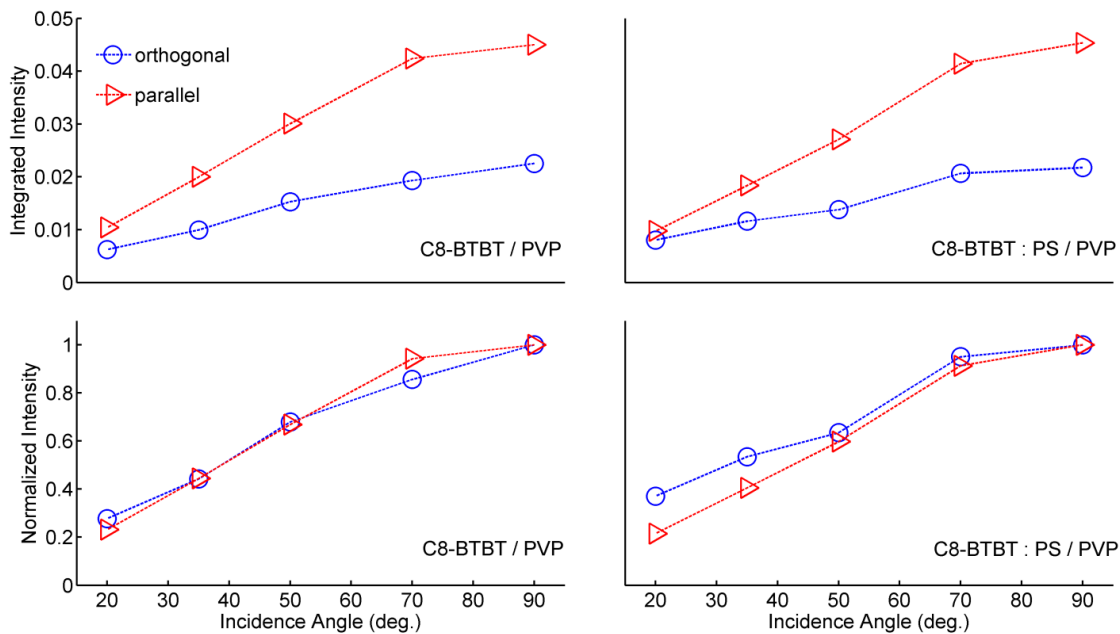
Supplementary Figure 9 | Dependence of the π^* intensity on the incident angle. The dependence of the integrated (top) and normalized (bottom) π^* intensity on the incident angle θ for two orthogonal orientations of the sample with respect to the dominant (in-plane) polarization direction of the elliptically-polarized X-ray beam. Blue circles (red triangles) represent the polarization direction of the X-ray is parallel (orthogonal) to the radial direction. The intensity differs by a factor of ~2 at 90 ° incidence, indicating a strong degree of in-plane crystal alignment.
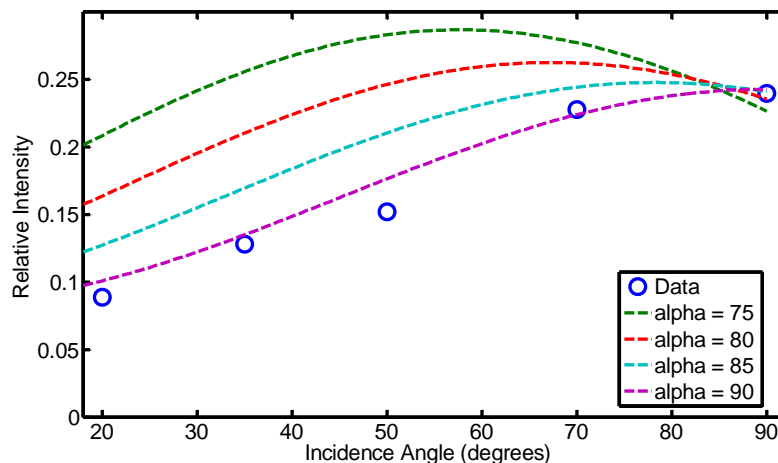
Supplementary Figure 10 | Calculated NEXAFS intensities with $\phi = 65^{\circ}$. The calculated NEXAFS intensity for a vector-type orbital with π symmetry as a function of incidence angle for different TDM tilt angles α and $\phi = 65^{\circ}$. The full intensity is plotted, i.e. the sum of the signal due to both polarization components of the incident electric field. The measured data is shown with blue open circles.
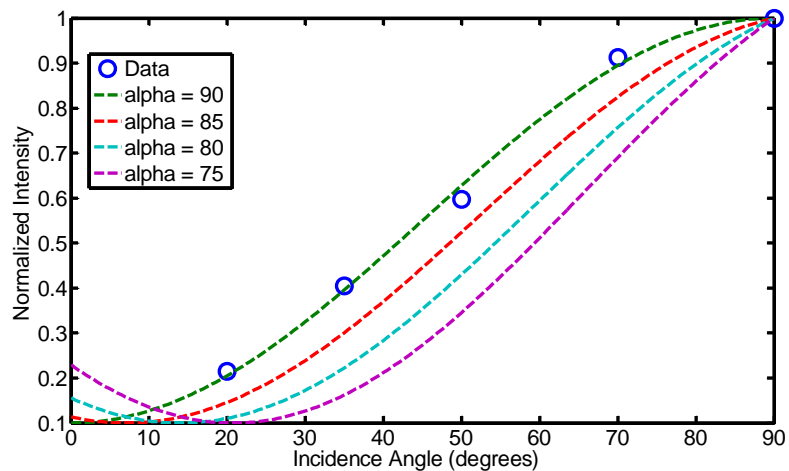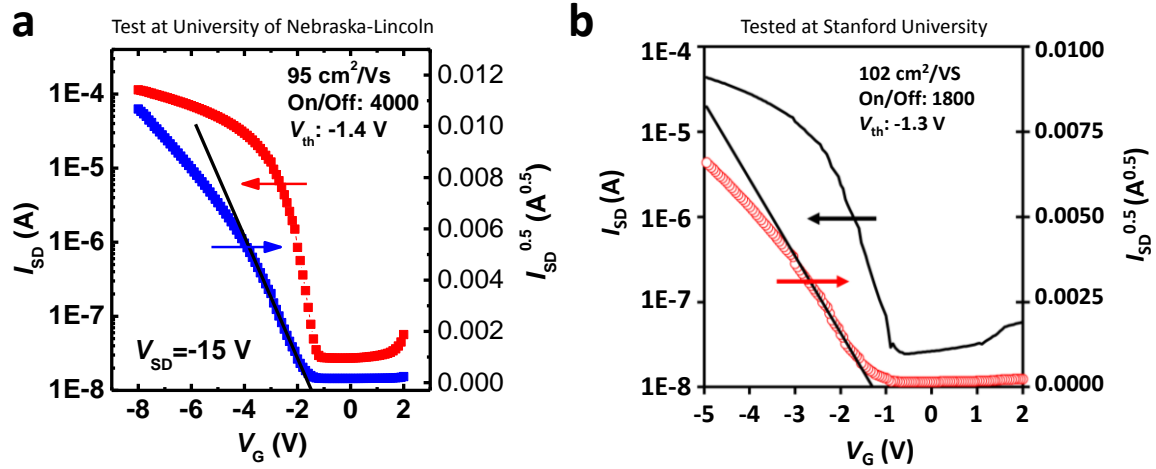
Supplementary Figure 11 | **Calculated NEXAFS intensities with** $\phi = 135^\circ$**.** The calculated

NEXAFS intensity for a vector-type orbital with π symmetry as a function of incidence angle for

different α and $\phi = 135^\circ$. The measured data is shown with blue open circles.
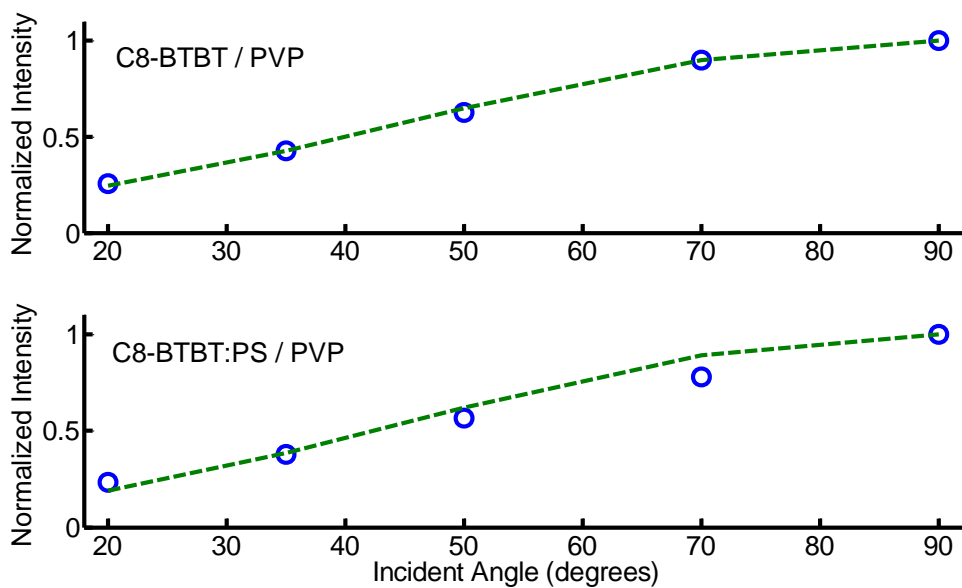
Supplementary Figure 12 | Fitting of the TDM tilt angles. Integrated π^* NEXAFS intensities vs. X-ray incidence angle (blue circles) and corresponding fits using Eq. S2 (green dashed line) for center-spun films. The top panel shows results for C8-BTBT/PVP and the bottom for C8-BTBT:PS/PVP. The calculated tilt angles of the TDM are 76.5 ° and 81 °, respectively. This translates into a tilt angle of the conjugated molecular core of 13.5 ° and 9 °, respectively.

a Test at University of Nebraska-Lincoln

95 cm^2/Vs
On/Off: 4000
V_{th}: -1.4 V

V_{SD}=-15 V

b Tested at Stanford University

102 cm^2/VS
On/Off: 1800
V_{th}: -1.3 V

Supplementary Figure 13 | Transfer curves of the occasionally measured ultra-high mobility around 100 cm^2/Vs. (a) I_{SD}-V_G curve tested in University of Nebraska-Lincoln and (**b**) verified in Stanford University.
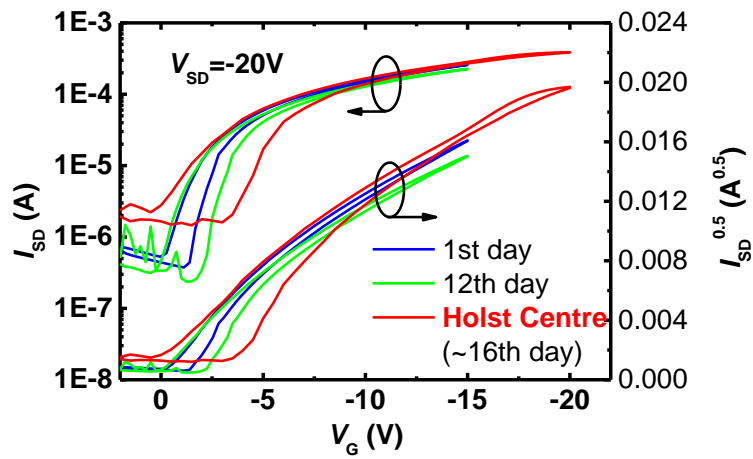
Supplementary Figure 14 | Transfer curve measured by different test system. The I_{SD}-V_G transfer curves have been measured in the University of Nebraska-Lincoln and Holst Centre, respectively.
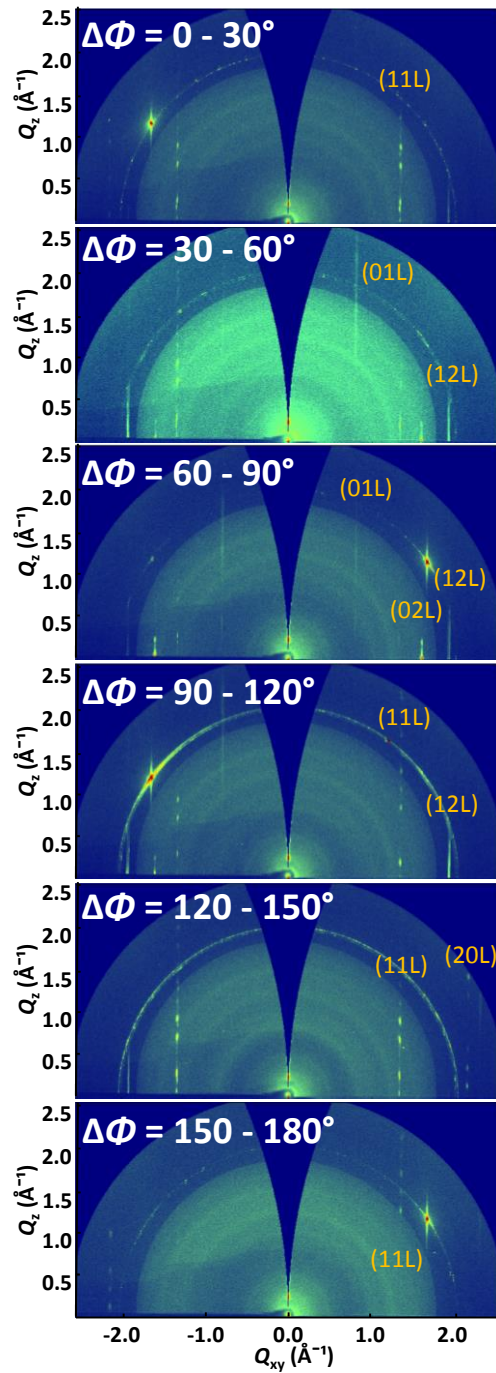
Supplementary Figure 15 | Anisotropic GIXD pattern of the OCSC C8-BTBT:PS film. The

GIXD images were obtained with a sample rotation step of 30 °.
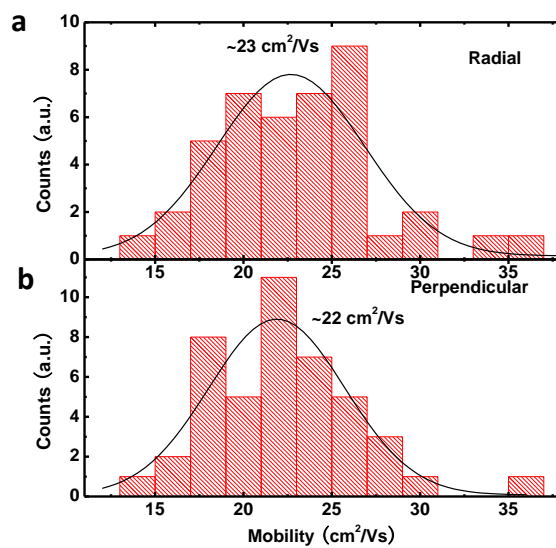
Supplementary Figure 16 | Isotropic hole mobilities in OCSC C8-BTBT:PS film. Distributions of the hole mobilities along: (**a**) the radial direction; and (**b**) the perpendicular direction.
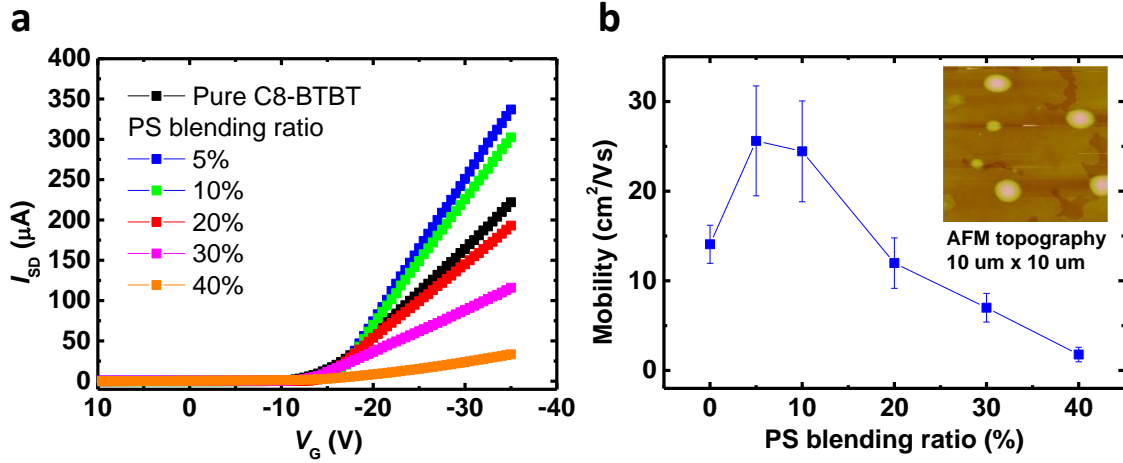
Supplementary Figure 17 | Influence of the PS blending on the hole mobilities. (**a**) Dependence of the channel current on the PS blending ratio; (**b**) Dependence of the hole mobility on the PS blending ratio. The inset is the AFM topography image of C8-BTBT:PS (70:30) film.
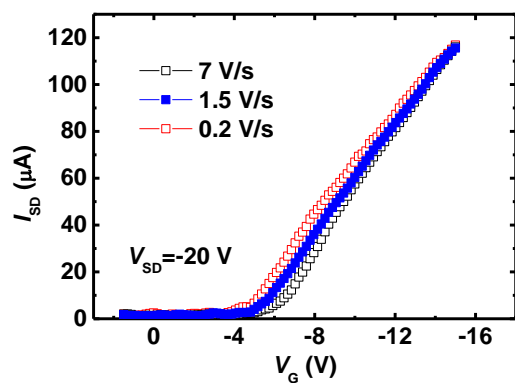
Supplementary Figure 18 | Channel current at different sweep rate. The channel current is not sensitive to the sweep rate from 0.2 V/s to 7 V/s.

Supplementary Table 1 | Influence of the fabrication method and PS blending on the hole mobilities.

Films fabrication method and solution used	Drop coating	OCSC
C8-BTBT without PS	~1 cm^2/Vs	~14 cm^2/Vs
C8-BTBT with PS	~4 cm^2/Vs	~25 cm^2/Vs

Supplementary Note 1 | Preferred growth direction of the OCSC C8-BTBT film.

The preferred growth direction has been identified by the GIXD measurement.[51] During the OCSC process, the C8-BTBT crystals grow along the radial direction. By comparing the anisotropic polarized absorption spectrum with reported spectrum,[18] the crystal growth direction is found to be parallel with the (010) direction along the radial casting direction. This observation was supported by GIXD results, where the sample was oriented with the incident X-ray beam along both the perpendicular and radial directions of casting, (Supplementary Figure 4a and b, respectively). The peaks are weak due to the film thinness as well as intensity degradation during the X-ray exposure. The (01L) and the (020) Bragg peaks are visible when the sample is positioned so that the perpendicular direction of the film and the X-ray beam are oriented in the same direction. This means the (010) direction is parallel the radial direction of the thin film. Similarly, the (100) direction is oriented along the perpendicular direction of casting.

Supplementary Note 2 | Asymmetric GIXD image of the OCSC C8-BTBT film.

Supplementary Figure 6 shows the GIXD image of C8-BTBT:PS film. The OCSC samples do not display symmetry with respect to the vertical axis of the image, and only a few Bragg peaks are visible compared to on-center spin-coated samples. This implies that only a few crystal planes meet the Bragg diffraction condition, indicating a large degree of in-plane alignment in the C8BTBT-PS off-center spin-coated sample. The (laterally) narrow peaks of the OCSC sample imply that the crystals have a large in-plane correlation length and are smaller than the sample length.

Supplementary Note 3 | NEXAFS measurement of the NEXAFS measurements

As mentioned in the supplementary method, we have been unable to precisely determine the unit cell packing of C8-BTBT due to X-ray beam-induced degradation. Near Edge X-ray Absorption Fine-structure Spectroscopy (NEXAFS)[52] can be collected much more rapidly than the time it takes to accurately collect intensities for a sufficient number of Bragg peaks for crystal structure refinement calculations. Consequently, beam damage is much less of a concern.

The theoretical intensities of the signal were calculated based on the formulas derived by Stöhr and Outka.[32] Within this formalism, the NEXAFS intensity for the dominant (in-plane) polarization component of the incident beam in the case of a vector-type π^* orbital is given by

$$I = \cos^2\theta\cos^2\alpha + \sin^2\theta\sin^2\alpha\cos^2\phi + \frac{1}{2}\sin 2\alpha\sin 2\theta\cos\phi \qquad (S1)$$

where θ is the X-ray incidence angle, α is the (polar) tilt angle of the transition dipole moment (TDM), and ϕ specifies the azimuthal (in-plane) orientation of the TDM. Since the C8-BTBT crystals in our films are highly bi-axially textured, the spectral intensity cannot be azimuthally averaged to integrate out the dependence on ϕ. For films with crystallites isotropically distributed in the substrate plane but with preferred orientation out of plane, i.e. 2D powders, Equation S1 must be averaged over ϕ to yield

$$I = \frac{1}{3}\left[1 + \frac{1}{2}(3\cos^2\theta - 1)(3\cos^2\alpha - 1)\right] \qquad (S2)$$

where, as mentioned above, I is the intensity of the dominant polarization component (in-plane). Supplementary Figure 8 shows the definition of all the angles.

NEXAFS is used here to calculate the orientation of the transition dipole moment of a specific absorption resonance, which can be related to the molecular tilt (polar) angle relative to the substrate plane. Although indirect, knowledge of the molecular tilt angle may be used to infer changes in the intermolecular transfer integral and thus the field-effect mobility. However, it must be borne in mind that in small molecule organic semiconductor crystals, there is frequently more than one molecule per unit cell. This is often the case with fused, linear conjugated molecules, which tend to exhibit herringbone packing. Thus, in the absence of *a priori* knowledge of the herringbone angle, the polar tilt angle obtained from NEXAFS will reflect an average over the distinct molecules in the unit cell.

Supplementary Figure 9 shows the integrated π^* intensity as a function of X-ray incidence angle for both pure C8-BTBT/PVP/Si and C8-BTBT:PS/PVP/Si samples. The top panels correspond to the integrated intensity, whereas the bottom panels show the same intensity but normalized by the value at $90°$ incidence.

The functional form of the normalized intensity as well as the absolute difference in intensities was modeled using Equation S1. We found that the functional form of the intensity vs. incident angle was qualitatively different from our data when the simulated tilt angle of the transition dipole moment dropped below $\sim85°$. That is, a peak develops in the intensity vs. incident angle curve that progressively moves to the middle of abscissa ($\phi < 90°$) as the TDM tilt angle decreases away from $90°$. This progression is shown in Supplementary Figure 10 ($\phi = 65°$) and S11 ($\phi = 135°$). For $\phi = 135°$, the appearance of the peak away from $90°$ incidence is evident in Supplementary Figure 11, which is qualitatively different from the functional form that we measure, where the intensity peaks near $90°$. Additionally, the difference in absolute

intensities at 90 ° cannot be captured by Supplementary Equation S1 when the TDM tilt angle starts to drop below 85 °. Based on this, we calculate a TDM tilt angle of ~88° with a rough error bar of ±3°. This corresponds to a tilt angle of the conjugated core of ~2°, i.e. a nearly perfectly edge-on configuration.

In order to compare NEXAFS results for off-center and on-center spun films, we have also measured NEXAFS spectra for the 2D powder samples (conventionally spin-coated). In this case, there is no difference between the measured intensities at different sample orientations owing to the isotropic distribution of crystallites in-plane. In this, Supplementary Equation S2 is used to fit the data and extract a tilt angle. Supplementary Figure 12 shows the data and the fits for C8-BTBT/PVP sample (top panel) and C8-BTBT:PS/PVP sample (bottom panel). We find that the tilt angles of the transition dipole moment are 76.5^o ($R^2 > 0.99$) and 81° ($R^2 = 0.95$), respectively. These values are lower than our calculations for the aligned off-center spun films, suggesting that the molecular packing and hence the intermolecular transfer integral differ between the two spin-coating methods.

Supplementary Note 4 | Surface energy difference of PVP, PS and C8-BTBT

The contact angle of cross-linked PVP (~64 °)[27] is closer to that of PS (66 °~85 °)[53,54] than that of C8-BTBT with long-chain alkyl groups, which usually lead to a contact angle of around 100 °.[55] C8-BTBT segregation on top helps to reduce the surface energy as compared to PS (~41 mJ/m^2) by the formation of methyl-terminated surface (~20 mJ/m^2).[56]

Supplementary Discussion

Polarized absorption spectroscopy. We observed a small spectral shift of ~50 meV between the peak positions of the first absorption band for the two different polarizations (Figure 1d). This corresponds to the Davydov splitting of the lowest energy transition in the isolated molecule due to the anisotropic crystal environment. The fact that the isolated molecular transition is split into two nearly orthogonally polarized components in the crystal suggests that there are two translationally inequivalent molecules per unit cell, consistent with single crystal structure data. To first order in perturbation theory, for absorption by free excitons in a crystal with two molecules per unit cell, the transition energy $\Delta E_{+,-}$ for the two Davydov components is given by

$$\Delta E_{+,-} = \Delta E_0 + D + I_{11} \pm I_{12}$$

Here, ΔE_0 is the transition energy of a single molecule. D is the difference in van der Waals energy between the ground and excited states; this is generally a negative quantity and thus tends to lower $\Delta E_{+,-}$, I_{11} and I_{12} are the sums of the coupling energies between pairs of molecules that are translationally equivalent and inequivalent, respectively.[57,58] The magnitude of the Davydov splitting is given by

$$\Delta E_+ - \Delta E_- = 2I_{12}$$

The interaction sums are defined with respect to the crystal ground and excited electronic states as follows:

$$I_{11} = \sum_q (\varphi_{1p}^* \varphi_{1q} | V_{1p,1q} | \varphi_{1p} \varphi_{1q}^*) \tag{S3}$$

$$I_{12} = {\sum_{q}}'(\varphi_{1p}^*\varphi_{2q}|V_{1p,2q}|\varphi_{1p}\varphi_{2q}^*) \qquad\qquad (S4)$$

The prime on the first sum indicates that the term with $q = p$ is excluded. φ_{1p} refers to the ground state wavefunction of molecule 1 (of 2) in unit cell p; φ_{1p}^* refers to the excited state wavefunction of the same molecule. $V_{1p,2q}$ is the interaction operator between molecule 1 in unit cell p and molecule 2 in unit cell q. Thus, Eq. S3 is the sum of interactions of all the molecules of the first kind (i.e. translationally equivalent) in the entire crystal, whereas Supplementary Equation S4 is the interaction sum for the translationally inequivalent molecules.

The onset of the absorption spectrum of the OCSC C8-BTBT:PS film shows a small blue shift of ~20 meV as compared to that of the small-angle drop-coated film. It is expected that these spectral differences would be correlated with a change in the crystal states of C8-BTBT. There are two factors that could explain the difference in the low-energy part of absorption spectrum between OCSC and drop-coated films: the van der Waals interaction between the excited electron and all the other electrons, and the interaction between transition dipoles corresponding to the two inequivalent molecules in the unit cell. It is likely that the interaction strength between transition dipoles of molecules in the unit cell and/or their mutual orientation changed upon thermal and solvent annealing, but this cannot currently be teased apart from the change in the van der Waals interaction. However, in either case it is expected that these optical changes would be correlated with a change in the molecular packing.

Verification of the high mobility device. The device performance was independent of the testing system used. High mobility devices have been verified in Stanford University and Holst Centre, respectively. Supplementary Figure 13 show the I_{SD}-V_G transfer curve of the occasionally

observed ultra-high mobility of about 100 cm^2/Vs tested in University of Nebraska-Lincoln and verified by the measurement system in Stanford University about 4 days later. Meanwhile, mobilities around 20~40 cm^2/Vs were more typically observed. Supplementary Figure 14 show the I_{SD}-V_G transfer curve of the typical high mobility device measured in University of Nebraska-Lincoln and Holst Centre. The high channel current can be repeated after 16 days, during which the device was stored in air and shipped to Holst Centre in the Netherlands. The off-current tested in Holst Centre increased compared to the fresh device; probably due to the probes slightly punch through the PVP dielectric layer. The hysteresis loop increased with storage time, which might be caused by the absorption of contaminants in air. For the verified device, the hole mobility fitted from the transfer curve (more than twenty data points were used for the linear fitting) is calculated to be 35 cm^2/Vs.

For the device with saturation mobility of 43 cm^2/Vs, the mobility calculated from the linear region at a V_G of -15 V is 20 cm^2/Vs (V_T: -11.5V and V_D: -5.5 V). The mobility fitted from the linear region might be underestimated because it is more strongly influenced by the contact resistance, especially when the mobility is high (>0.1 cm^2/Vs) or the channel length is short.[59-61] In our case, the contact resistance is expected to be large, due to there are a high injection barrier at C8-BTBT/Ag interface of about 1 eV and long-chain alkyl groups on both side of the C8-BTBT molecule.

Crystal orientation and isotropic mobility. As for the crystal orientation, we found there is a significant orientation of the C8-BTBT films, as show in Supplementary Figures 4 & 15. In Supplementary Figure 15, different Bragg peaks were obtained when the sample rotated with a step of 30 °, as different crystal planes meet the diffraction condition, indicating the crystals are

highly aligned. This observation is consistent with the polarization absorption spectrum as shown in Figure 1d and the NEXAFS.

Meanwhile, the hole mobility along radial and perpendicular directions has been determined by depositing the electrode patterns with a channel direction parallel or perpendicular to the radial direction. However, as shown in Supplementary Figure 16, the hole carrier nobilities along the radial direction (average value: 23 cm^2/Vs, standard deviation: 8.3 cm^2/Vs) and the perpendicular direction (average value: 22 cm^2/Vs, standard deviation: 7.7 cm^2/Vs) were found to be the same. The nearly equal mobilities are reasonable because the charge transfer integrals at different directions are roughly balanced.[16,24] The fact that the mobility is nearly isotropic suggests that the measured larger mobility values relative to previous studies are not primarily caused by the anisotropic charge-transport nature of the C8-BTBT crystal.

Ratio dependence of C8-BTBT:PS blend. As an insulating polymer, the content of PS in the C8-BTBT solution is crucial for the optimizing of carrier mobility. The influence of the PS blending ratio on the device mobility has been studied (Supplementary Figure 17). When 5-10 wt% of PS was added, the average mobility (>6 samples were taken for the consideration) of the resulting TFTs improved from ~14 cm^2/Vs to ~25 cm^2/Vs. The mobility began to decrease as the PS concentration was increased to 10 wt%. When the PS concentration was increased to 20 wt%, the resulting mobility decreased below that of the pure C8-BTBT thin film. The drop of the mobility is mainly caused by two reasons: the reduced continuity of the C8-BTBT film due to the less content of C8-BTBT; and the formation of micrometer scale insulating PS domains with heights in several tens of nanometer-scale due to an excessive PS content (Supplementary Figure 17b, inset), which form barriers for the carrier transport.

TEM cross section image of pure C8-BTBT and C8-BTBT:PS films. In a conventional (unfiltered) cross-sectional TEM view, C8-BTBT film is visible as a dark thin layer with 10-20 nm thickness, due to its high crystallinity and electron density (Figure 4a). An additional thinner layer ($\leq$5 nm) is somewhere visible between the C8-BTBT layer and the substrate (Figure 4a). We attribute this ultrathin layer to PS based on its relative small concentration in the blend and low electron density associated with its amorphous structures. We further confirmed the existence of this ultrathin PS layer by using energy filtered TEM (Figure 4b). The 22$\pm$4 eV image has enhanced contrast because the low eV electron energy loss spectra (EELS) of p-type organic semiconductors have a plasmon peak in this energy range.[39,40] A corresponding thickness map is obtained by the ratio of unfiltered and filtered image, yielding pixel by pixel values of t/λ, where t is film thickness in nanometer and λ is the mean free pathway of electron. Both 22$\pm$4 eV image and thickness map suggest that there is an additional layer underneath C8-BTBT.

SEM cross section image of C8-BTBT:PS film. In order to demonstrate the PS is more likely attached to the PVP surface during the vertical phase separation process, the C8-BTBT:PS blend was drop coated on the PVP surface to form thick film and then studied by SEM. The PS blending ratio was improved to 50% to make the pure PS film more easily to be found. Figure 4c show the SEM cross section image of the C8-BTBT:PS film drop coated on PVP surface. This section was obtained by cooling the samples with liquid nitrogen and then breaking off the sample immediately. Since the PS is more flexible than the C8-BTBT crystal, the section of PS layer is not as smooth as that of C8-BTBT layer, it extended out of the section and can be identify easily. The SEM image clearly shows that a continuous PS layer was formed and preferred to segregate on the PVP surface.

Mobility of OTFTs with different sweep rate. In this study, no obvious sweep rate-dependent mobility was observed. As shown in Supplementary Figure 18, where the mobilities obtained at 7 V/s, 1.5 V/s and 0.2 V/s were 28 cm^2/Vs, 26 cm^2/Vs and 27 cm^2/Vs, respectively. The variation is only around 5%, showing the device has a negligible trap state density and thus robust stress bias stability.

Supplementary Methods

Fabrication and optical measurement of drop-coating C8-BTBT film. In our experiment, the

C8-BTBT film in Figure 1d (black line) was fabricated by an small-angle drop-coating method,[30]

where the substrate was tilted by ~3 ° and heated up to 80 ℃. During the drying process, DCB

solvent annealing was used to slow down the drying process and adequately improve the

crystallinity. More specifically, the sample was covered by a glass petri dish full of DCB vapor.

The molecules have a much longer time to form the end-state crystal lattice in the small-angle

drop-coating method relative to the spin-coating technique. The C8-BTBT film grows

anisotropically and form crystal domains in mm scale. Then the polarized absorption

measurement was carried on the large C8-BTBT crystal domain, as selected by polarized optical

microscopy. The drop-coating method mentioned in Figure 3e,f was different, where the C8-

BTBT:PS solution was drop-coated at 20 ℃, and after dripping the C8-BTBT:PS solution onto

the substrate, the substrate was tilted immediately by a large degree (e.g. ~90 °); during the

drying process, a continuous airflow was used to carry away the DCB vapor. There are three

ranges of thickness discussed in this work which were obtained by three different methods:

   1. Very thin C8-BTBT film (10~18 nm): by OCSC method;

   2. Thin C8-BTBT film (15~50 nm, Figure 3e,f): by large-angle drop-coating;

   3. Thick C8-BTBT film (>50 nm, Figure 1d): by small-angle drop-coating combining with
      thermal and DCB solvent annealing.

The method 3 in Figure 1d assures a film without measurable metastable polymorphs because

there is little force to drive its formation and the film was thermally and DCB-vapor

annealed. Both the gravity force in the large tilting angle drop-coating and a centrifugal force in

the high speed spin-coating process results in the formation of metastable polymorph. And the metastable phase percentage decrease from method 1 to method 3. This can explain the larger carrier mobility of the drop-casted films with reduced thickness.

GIXD measurement. The meta-stable structure of the C8-BTBT film has been studied by the GIXD measurement. In-situ thermal annealing was performed by placing the sample on a stage with a heater. Samples were held at 90 ^{o}C for at least 5 mins to melt the C8-BTBT crystallites. GIXD images of the same region were taken before heating, when the substrate was at 90 ℃, and after cooling, in order to study crystal structure and texture change.

The in-plane coherence length by Scherrer analysis provided a lower bound crystallite size of ~100 nm, which was limited by sample degradation upon X-ray beam exposure (Supplementary Figure 5). Besides, unfortunately, due to the beam degradation of the sample upon long X-ray exposure times, we were unable to obtain the precise crystal structure.

The meta-stable C8-BTBT films were heated up to 90 ℃ in order to access the liquid crystalline phase and erase history of the metastable packing phase (Figure 2c and Supplementary Figure 7).[62] The in-plane Bragg peaks disappeared when the sample was heated to 90 ℃, indicating that the thin film at 90 ℃ did not possess any long-range in-plane order. When this sample was cooled back down to room temperature, the Bragg peak re-appeared at a slightly shifted reciprocal space (Q_{xy}) position. The sample was fixed during the in-situ annealing processes, thus eliminating any error in the real sample to detector distance. We assign the peak position and intensity changes to the change in the underlying crystal packing motif and texture. We hence interpret the pre-thermal anneal peak as indication of a meta-stable packing phase.

Supplementary References

53 Guruvenket, S., Rao, G. M., Komath, M. & Raichur, A. M. Plasma surface modification of polystyrene and polyethylene. *Appl. Surf. Sci.* **236**, 278-284 (2004).

54 Li, Y., Pham, J. Q., Johnston, K. P. & Green, P. F. Contact angle of water on polystyrene thin films: Effects of CO_2 environment and film thickness. *Langmuir* **23**, 9785-9793 (2007).

55 Fadeev, A. Y. & McCarthy, T. J. Self-assembly is not the only reaction possible between alkyltrichlorosilanes and surfaces: monomolecular and oligomeric covalently attached layers of dichloro-and trichloroalkylsilanes on silicon. *Langmuir* **16**, 7268-7274 (2000).

56 Collet, J., Tharaud, O., Chapoton, A. & Vuillaume, D. Low-voltage, 30 nm channel length, organic transistors with a self-assembled monolayer as gate insulating films. *Appl. Phys. Lett.* **76**, 1941-1943 (2000).

57 Craig, D. P. & Walmsley, S. *Excitons in molecular crystals: theory and applications*. (Benjamin, 1968).

58 Davydov, A. S. & Dresner, S. B. *Theory of molecular excitons*. Vol. 1 (Plenum Press New York, 1971).

59 Dimitrakopoulos, C. D. & Mascaro, D. Organic thin-film transistors: A review of recent advances. *IBM Journal of Research and Development* **45**, 11-27 (2001).

60 Zaumseil, J., Baldwin, K. W. & Rogers, J. A. Contact resistance in organic transistors that use source and drain electrodes formed by soft contact lamination. *J. Appl. Phys.* **93**, 6117-6124 (2003).

61   Malenfant, P. R. L. *et al.* N-type organic thin-film transistor with high field-effect mobility based on a N, N-dialkyl-3, 4, 9, 10-perylene tetracarboxylic diimide derivative. *Appl. Phys. Lett.* **80**, 2517 (2002).

62   Iino, H. & Hanna, J. Availability of Liquid Crystallinity in Solution Processing for Polycrystalline Thin Films. *Adv. Mater.* **23**, 1748-1751 (2011).